Trajectory Challenges Faced By Reusable Infrastructure In Earth Orbit Supporting Multiple Departures For Mars

1. Introduction

Imagine infrastructure in a prograde circular low Earth orbit (LEO) whose primary purpose is to assemble and service massive payloads for Mars departures during multiple departure seasons. Assume each departure is accomplished with one trans-Mars injection (TMI) burn at sufficiently high thrust that it may be modeled impulsively with reasonable accuracy. Under this assumption, a Mars departure season typically lasts about a month, and successive seasons arise once every Mars synodic period such that they are centered about 26 months apart.

Interplanetary trajectories reported in this paper typically see initial definition as geocentric or heliocentric conic loci and are "blended" together using patched conic theory. Ultimately, all trajectories influencing this paper's results are modeled via numeric integration [1] of gravity accelerations exerted by the Earth, the Moon, and the Sun. Whenever within Earth's gravitational sphere of influence (at geocentric distances less than about 1 million km), trajectory modeling also reflects acceleration accounting for Earth's excess equatorial mass, known as the J_2 harmonic. Atmospheric drag experienced by the LEO infrastructure is intentionally omitted from trajectory modeling to avoid vehicle-specific results and to approximate an altitude maintenance strategy preserving infrastructure design lifetime.

This paper assumes the departure LEO is initially at inclination $i = 29°$ with respect to Earth's true equator and at height $H = +400$ km with respect to an Earth equatorial radius $r_E = 6378.136$ km [2] such that $r \equiv H + r_E = 6778.136$ km*. The LEO plane is oriented to target an in-plane, single-impulse TMI on 14.0 July 2020 UT resulting in a Type 1 "short way" Mars intercept on 30.0 January 2021 UT with the associated transfer ellipse from Earth subtending a heliocentric angle less than 180°. A celestial sphere plot (CSP) is used to graphically illustrate geometric constraints governing this in-plane departure.

After the 14.0 July 2020 departure, the infrastructure is coasted in LEO until the next Mars departure season and compared to an ideal LEO with near-minimal i leading to an in-plane, single-impulse TMI on 9.0 September 2022 UT. This TMI solution results in a Type 1 Mars intercept on 28.0 March 2023 UT. A CSP is again applied to illustrating the planar mismatch between the coasted LEO from 2020 and the ideal Mars departure LEO in 2022. Strategies for minimizing this mismatch are then suggested.

2. Earth Departure Geometric Constraints

Orientation of the infrastructure's LEO plane is constrained at Earth departure by geocentric asymptotic velocity $\boldsymbol{v}_\infty$ associated with the selected Type 1 heliocentric transfer ellipse from Earth to Mars. When Earth heliocentric velocity is subtracted from heliocentric velocity in the transfer ellipse at the Earth departure date, $\boldsymbol{v}_\infty$ results. In order to provide an efficient in-plane TMI burn, the LEO plane must contain $\boldsymbol{v}_\infty$.

---

* Apogee and perigee heights H_A and H_P reported in this paper are referred to r_E and analytically account for J_2 perturbations [3].

This paper reports $\boldsymbol{v}_\infty$ Cartesian components reckoned with respect to the geocentric Earth mean equator and equinox of epoch J2000.0 (J2K) coordinate system. In practice, a sufficiently accurate $\boldsymbol{v}_\infty$ is computed from the conic heliocentric transfer ellipse determined by solving a Lambert boundary value problem. Along with specifying a Type 1 heliocentric transfer, boundary values defining this Lambert problem are Earth's heliocentric position at Earth departure, Mars's heliocentric position at Mars arrival, and the time-of-flight between departure and arrival.

As vividly illustrated in [4] on pp. 114-115, $\boldsymbol{v}_\infty$ is the axis of symmetry for a manifold of geocentric Earth departure hyperbolas leading to the desired Type 1 heliocentric transfer. This manifold in turn defines a locus of possible injection points (LPIP) for TMI as illustrated in Figure 1. The LPIP is a small circle whose radius subtends a geocentric angle equal to β (called the asymptote angle) and whose center lies in the -$\boldsymbol{v}_\infty$ direction.

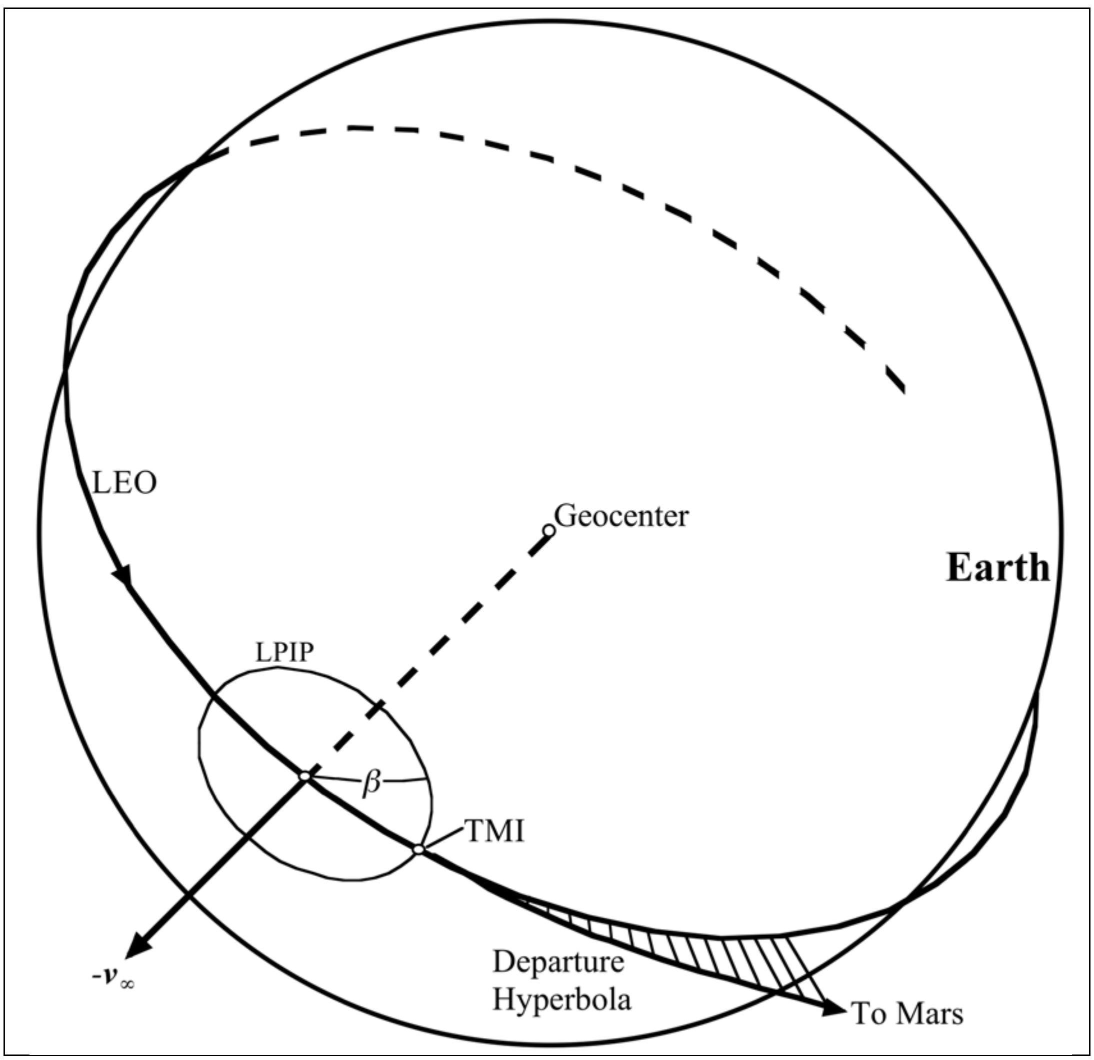

Figure 1. Earth departure geometry for Mars is constrained by -v_∞. As the departure hyperbola approaches interplanetary space, velocity will approach +v_∞.

Generic departure geometry illustrated in Figure 1 adopts a conventional perspective looking down on Earth's surface from above. To illustrate specific departure geometries developed by this paper, however, geocentric vectors and planes are instead *projected* onto the J2K celestial sphere whose radius is effectively infinite. These CSPs are similar to conventional maps with longitude replaced by J2K right ascension in the horizontal direction, and latitude replaced by J2K declination in the vertical direction. Although north is still upward on a CSP, it should be noted east is to the left because the celestial sphere is being viewed from the geocenter looking outward at its *inside*. Consequently, infrastructure motion in its prograde LEO will be from right to left on a CSP.

Starting in the infrastructure's LEO immediately prior to TMI, a Mars-bound payload first coasts through a geocentric position in the $-\boldsymbol{v}_\infty$ direction. It then coasts through an arc subtending β before arriving at the TMI point[†]. Because this point is also perigee in a geocentric Earth departure hyperbola coplanar with the LEO, impulsive TMI change in velocity magnitude Δv_{TMI} is minimal. Under this geometry, TMI velocity change will be a purely prograde impulse with zero radial and out-of-plane components.

With the LEO plane constrained to contain $\boldsymbol{v}_\infty$, the LEO's i is also constrained as a consequence. If the declination δ_∞ of $\boldsymbol{v}_\infty$ with respect to Earth's true equator is computed, i must be greater than or equal to $| \delta_\infty |$. In this paper, launches to the LEO-resident infrastructure from a true declination at +28.5° are assumed, a value near that for Cape Canaveral, Florida. To maximize payload mass per launch under this assumption, i will be selected no less than 29° or slightly greater than $| \delta_\infty |$, whichever value is greater.

At a prograde $i > | \delta_\infty |$, there are two LEO planes passing through a geocentric position in the $-\boldsymbol{v}_\infty$ direction. One plane will satisfy this condition on a northbound heading $0 < \psi < 90°$ east of true north at TMI, and one will satisfy it on a southbound heading $90° < \psi < 180°$ east of true north at TMI. The LEO plane with northbound TMI is arbitrarily selected in lieu of compelling rationale to the contrary.

3. Earth Departure Date And LEO Inclination Selection

Earth departure date and infrastructure LEO i selection are facilitated by pork chop charts (PCCs). In this paper's context, a PCC is a two-dimensional matrix of values from an ordered array of Type 1 Lambert solutions each having Earth departure date t_D and Mars arrival date t_A. The value assigned to each solution in the matrix maps a third dimension and may be any single variable relatable to all the solutions. Matrix elements having t_D later than the corresponding t_A are left blank (no value is assigned).

[†] If this geometry is applied to planetary arrival, its description is somewhat altered. The arriving payload coasts to periapsis along its planetocentric approach hyperbola, where a retrograde orbit insertion impulse is applied. After coasting in the insertion orbit through a planetocentric arc subtending β, the payload passes through a planetocentric position in the $+\boldsymbol{v}_\infty$ direction.

Trajectory Challenges Faced By Reusable Infrastructure In Earth Orbit Supporting Multiple Departures For Mars

By convention, a PCC's columns increment from left-to-right with increasing t_D, and its rows increment from top-to-bottom with increasing t_A. Per the previous section's Earth departure geometric constraints, values assigned to each PCC matrix element are $| \boldsymbol{v}_\infty |$ or δ_∞. Values in a PCC are color-coded to indicate low (green), medium (pink), or high (red) magnitudes. When $\left| \boldsymbol{v}_\infty \right|$ values are assigned, the low/medium threshold is 4 km/s, and the medium/high threshold is 6 km/s. For $| \delta_\infty |$, the low/medium threshold is 28.5°, and the medium/high threshold is 57°.

The PCC pair governing selection of the 2020 Earth departure case appears in Figures 2 and 3. A notional 10-day departure season is boxed, but the actual departure case is the season-opening t_D at 14.0 July 2020 UT with $| \boldsymbol{v}_\infty |$ = 3.665 km/s. Since δ_∞ = +26.822° for this case, i = 29° is selected.

◇	A	B	C	D	E	F	G	H	I	J	K	L	M	N	O	P	Q	R	S	T
1	Mars Arrive									Earth Depart Date										
2	Date	4/25/20	5/5/20	5/15/20	5/25/20	6/4/20	6/14/20	6/24/20	7/4/20	7/14/20	7/24/20	8/3/20	8/13/20	8/23/20	9/2/20	9/12/20	9/22/20	10/2/20	10/12/20	10/22/20
3	5/5/20	208.536																		
4	5/15/20	99.212	195.961																	
5	5/25/20	63.285	93.045	183.769																
6	6/4/20	45.590	59.241	87.063	171.956															
7	6/14/20	35.105	42.610	55.313	81.260	160.588														
8	6/24/20	28.177	32.771	39.708	51.490	75.693	149.591													
9	7/4/20	23.260	26.281	30.491	36.870	47.830	70.290	138.967												
10	7/14/20	19.599	21.685	24.422	28.245	34.153	44.263	65.065	128.772											
11	7/24/20	16.781	18.267	20.133	22.578	26.095	31.494	40.804	60.070	118.941										
12	8/3/20	14.562	15.640	16.949	18.579	20.808	23.979	28.904	37.509	55.245	109.538									
13	8/13/20	12.791	13.574	14.506	15.618	17.087	19.058	21.907	26.444	34.323	50.661	100.679								
14	8/23/20	11.363	11.926	12.588	13.351	14.337	15.602	17.334	19.945	24.065	31.317	46.411	92.415							
15	9/2/20	10.208	10.598	11.060	11.574	12.237	13.056	14.131	15.707	18.048	21.839	28.588	42.525	85.016						
16	9/12/20	9.276	9.524	9.830	10.160	10.595	11.118	11.780	12.750	14.137	16.293	19.872	26.166	39.224	78.810					
17	9/22/20	8.529	8.655	8.836	9.025	9.292	9.608	9.998	10.589	11.421	12.704	14.794	18.198	24.264	36.728	74.165				
18	10/2/20	7.945	7.954	8.030	8.108	8.249	8.414	8.616	8.961	9.450	10.231	11.534	13.595	17.035	23.070	35.254	71.663			
19	10/12/20	7.520	7.393	7.380	7.368	7.410	7.463	7.531	7.709	7.979	8.458	9.318	10.681	12.916	16.549	22.736	35.138	71.722		
20	10/22/20	7.320	6.954	6.856	6.770	6.734	6.701	6.672	6.734	6.862	7.154	7.758	8.740	10.364	12.900	16.840	23.481	36.480	74.581	
21	11/1/20	8.305	6.624	6.438	6.290	6.191	6.092	5.990	5.971	6.004	6.183	6.639	7.411	8.710	10.690	13.591	18.035	25.261	39.276	80.280
22	11/11/20	61.926	6.424	6.107	5.907	5.758	5.606	5.449	5.373	5.345	5.456	5.830	6.490	7.615	9.291	11.648	15.044	20.005	27.988	43.436
23	11/21/20	62.101	7.214	5.846	5.606	5.416	5.222	5.024	4.907	4.839	4.913	5.246	5.850	6.880	8.382	10.425	13.244	17.086	22.641	31.557
24	12/1/20	62.059	62.011	5.640	5.377	5.154	4.924	4.693	4.547	4.453	4.509	4.826	5.405	6.383	7.777	9.623	12.089	15.292	19.616	25.852
25	12/11/20	61.980	61.995	42.488	5.243	4.967	4.702	4.442	4.273	4.163	4.212	4.525	5.095	6.043	7.365	9.075	11.306	14.104	17.709	22.565
26	12/21/20	61.869	61.949	61.932	5.672	4.880	4.555	4.263	4.072	3.950	3.997	4.312	4.878	5.806	7.074	8.685	10.747	13.268	16.409	20.451
27	12/31/20	61.727	61.871	61.930	60.705	5.077	4.501	4.153	3.935	3.800	3.844	4.161	4.725	5.636	6.860	8.393	10.327	12.646	15.466	18.978
28	1/10/21	61.555	61.763	61.888	61.852	7.979	4.633	4.125	3.859	3.704	3.741	4.055	4.614	5.508	6.694	8.162	9.995	12.158	14.742	17.887
29	1/20/21	61.352	61.624	61.814	61.881	60.801	5.456	4.229	3.852	3.658	3.679	3.984	4.533	5.408	6.559	7.971	9.718	11.758	14.161	17.035
30	1/30/21	61.121	61.456	61.708	61.848	61.760	12.527	4.652	3.940	3.665	3.652	3.939	4.473	5.325	6.443	7.804	9.479	11.416	13.674	16.341
31	2/9/21	60.863	61.259	61.573	61.779	61.819	60.713	6.246	4.207	3.741	3.664	3.918	4.428	5.255	6.338	7.653	9.263	11.113	13.251	15.753
32	2/19/21	60.577	61.034	61.408	61.677	61.797	61.721	17.393	4.913	3.925	3.721	3.920	4.396	5.192	6.241	7.511	9.063	10.837	12.874	15.241
33	3/1/21	60.266	60.782	61.216	61.546	61.733	61.812	60.518	7.149	4.323	3.845	3.951	4.378	5.136	6.148	7.376	8.875	10.581	12.530	14.782
34	3/11/21	59.930	60.504	60.996	61.386	61.636	61.801	61.693	20.520	5.237	4.083	4.020	4.375	5.087	6.060	7.245	8.694	10.338	12.209	14.362
35	3/21/21	59.569	60.201	60.749	61.198	61.508	61.742	61.822	60.172	7.839	4.547	4.152	4.395	5.047	5.976	7.118	8.519	10.106	11.907	13.973
36	3/31/21	59.186	59.873	60.477	60.983	61.351	61.648	61.823	61.647	21.219	5.544	4.394	4.448	5.018	5.896	6.994	8.348	9.882	11.619	13.607
37	4/10/21	58.780	59.521	60.180	60.743	61.168	61.523	61.770	61.820	59.647	8.188	4.853	4.557	5.007	5.823	6.873	8.181	9.665	11.342	13.259
38	4/20/21	58.353	59.147	59.859	60.477	60.957	61.369	61.680	61.835	61.641	19.989	5.812	4.766	5.024	5.759	6.757	8.017	9.453	11.074	12.926
39	4/30/21	57.905	58.750	59.514	60.186	60.721	61.189	61.559	61.788	61.872	58.677	8.238	5.168	5.088	5.710	6.646	7.857	9.245	10.813	12.605
40	5/10/21	57.436	58.332	59.147	59.871	60.460	60.981	61.408	61.702	61.902	61.627	17.798	6.008	5.235	5.684	6.543	7.702	9.043	10.560	12.295
41	5/20/21	56.948	57.892	58.757	59.532	60.174	60.748	61.231	61.583	61.861	61.936	56.751	8.064	5.543	5.694	6.452	7.551	8.844	10.312	11.993
42	5/30/21	56.442	57.432	58.345	59.171	59.864	60.490	61.026	61.434	61.777	61.984	61.569	15.357	6.204	5.770	6.378	7.408	8.650	10.070	11.699
43	6/9/21	55.916	56.952	57.912	58.787	59.530	60.207	60.796	61.258	61.659	61.949	61.987	52.732	7.811	5.970	6.333	7.273	8.462	9.832	11.412
44	6/19/21	55.373	56.453	57.458	58.381	59.173	59.900	60.541	61.056	61.512	61.868	62.055	61.510	13.089	6.437	6.336	7.152	8.279	9.600	11.131
45	6/29/21	54.812	55.935	56.983	57.953	58.793	59.569	60.261	60.827	61.336	61.751	62.026	62.089	44.513	7.595	6.429	7.051	8.103	9.372	10.856
46	7/9/21	54.234	55.397	56.488	57.503	58.391	59.214	59.956	60.573	61.134	61.604	61.945	62.179	61.366	11.237	6.711	6.984	7.937	9.150	10.586
47	7/19/21	53.640	54.842	55.974	57.033	57.966	58.836	59.627	60.294	60.905	61.429	61.829	62.153	62.196	32.797	7.469	6.978	7.786	8.934	10.321
48	7/29/21	53.028	54.268	55.439	56.541	57.519	58.435	59.274	59.989	60.650	61.226	61.681	62.073	62.312	61.052	9.843	7.096	7.656	8.725	10.060
49	8/8/21	52.401	53.677	54.886	56.029	57.050	58.011	58.896	59.660	60.370	60.996	61.503	61.954	62.289	62.293	22.666	7.518	7.565	8.525	9.805
50	8/18/21	51.757	53.068	54.313	55.496	56.560	57.564	58.495	59.306	60.064	60.740	61.298	61.803	62.207	62.435	60.460	8.931	7.551	8.340	9.555

Figure 2. Values of $| v_\infty |$ targeting Mars are tabulated for year 2020 Earth departure dates. The 14.0 July 2020 UT opening date of a notional 10-day departure season (boxed) has $| v_\infty |$ = 3.665 km/s and is selected for assessment.

◇	A	B	C	D	E	F	G	H	I	J	K	L	M	N	O	P	Q	R	S	T
1	Mars Arrive									Earth Depart Date										
2	Date	4/25/20	5/5/20	5/15/20	5/25/20	6/4/20	6/14/20	6/24/20	7/4/20	7/14/20	7/24/20	8/3/20	8/13/20	8/23/20	9/2/20	9/12/20	9/22/20	10/2/20	10/12/20	10/22/20
3	5/5/20	-15.001																		
4	5/15/20	-12.896	-12.845																	
5	5/25/20	-10.828	-10.611	-10.579																
6	6/4/20	-8.920	-8.440	-8.257	-8.259															
7	6/14/20	-7.258	-6.453	-6.023	-5.902	-5.936														
8	6/24/20	-5.886	-4.732	-3.993	-3.655	-3.593	-3.653													
9	7/4/20	-4.813	-3.314	-2.242	-1.628	-1.383	-1.370	-1.474												
10	7/14/20	-4.030	-2.203	-0.803	0.110	0.595	0.762	0.692	0.555											
11	7/24/20	-3.520	-1.385	0.324	1.532	2.278	2.654	2.692	2.556	2.390										
12	8/3/20	-3.265	-0.834	1.162	2.645	3.646	4.252	4.449	4.378	4.180	3.966									
13	8/13/20	-3.251	-0.523	1.743	3.475	4.711	5.543	5.918	5.956	5.783	5.489	5.252								
14	8/23/20	-3.470	-0.424	2.102	4.062	5.506	6.544	7.092	7.257	7.146	6.816	6.466	6.202							
15	9/2/20	-3.926	-0.512	2.279	4.449	6.075	7.292	7.995	8.281	8.247	7.907	7.474	7.063	6.768						
16	9/12/20	-4.640	-0.764	2.312	4.683	6.469	7.837	8.666	9.054	9.091	8.749	8.249	7.706	7.227	6.948					
17	9/22/20	-5.675	-1.163	2.243	4.815	6.742	8.235	9.161	9.621	9.709	9.353	8.783	8.112	7.453	7.000	6.741				
18	10/2/20	-7.187	-1.697	2.117	4.900	6.953	8.546	9.538	10.039	10.147	9.751	9.093	8.285	7.444	6.825	6.414	6.217			
19	10/12/20	-9.606	-2.377	1.989	5.003	7.169	8.836	9.863	10.371	10.463	9.990	9.214	8.247	7.218	6.448	5.914	5.634	5.566		
20	10/22/20	-14.412	-3.266	1.922	5.200	7.465	9.178	10.208	10.684	10.722	10.129	9.195	8.044	6.826	5.929	5.312	5.000	4.953	4.996	
21	11/1/20	-30.257	-4.589	2.013	5.596	7.930	9.654	10.649	11.054	10.994	10.234	9.101	7.744	6.343	5.353	4.701	4.409	4.433	4.567	4.738
22	11/11/20	15.384	-7.354	2.439	6.347	8.684	10.358	11.270	11.557	11.353	10.378	9.006	7.426	5.859	4.814	4.171	3.941	4.068	4.322	4.646
23	11/21/20	18.871	-24.781	3.667	7.736	9.896	11.410	12.165	12.275	11.875	10.634	8.987	7.176	5.465	4.395	3.790	3.643	3.888	4.273	4.754
24	12/1/20	19.129	17.209	7.962	10.409	11.848	12.969	13.446	13.295	12.635	11.076	9.118	7.069	5.229	4.149	3.591	3.531	3.891	4.402	5.032
25	12/11/20	18.984	17.328	61.609	16.381	15.092	15.280	15.252	14.712	13.708	11.768	9.461	7.162	5.193	4.099	3.582	3.596	4.056	4.679	5.443
26	12/21/20	18.706	16.992	15.907	36.282	20.938	18.763	17.777	16.636	15.168	12.770	10.063	7.490	5.376	4.247	3.749	3.817	4.357	5.073	5.950
27	12/31/20	18.366	16.566	14.938	22.327	33.326	24.239	21.320	19.207	17.096	14.134	10.959	8.071	5.777	4.581	4.075	4.171	4.767	5.557	6.526
28	1/10/21	17.990	16.107	14.245	13.455	65.768	33.532	26.389	22.627	19.587	15.913	12.177	8.914	6.392	5.087	4.539	4.635	5.265	6.106	7.147
29	1/20/21	17.590	15.630	13.623	11.971	17.784	50.918	33.906	27.198	22.768	18.166	13.745	10.024	7.212	5.750	5.125	5.191	5.831	6.704	7.798
30	1/30/21	17.174	15.144	13.031	11.044	10.448	77.985	45.571	33.410	26.822	20.973	15.695	11.411	8.233	6.560	5.818	5.827	6.453	7.339	8.466
31	2/9/21	16.746	14.651	12.454	10.282	8.647	14.259	63.693	42.043	32.017	24.444	18.074	13.092	9.456	7.510	6.611	6.531	7.121	8.001	9.145
32	2/19/21	16.307	14.153	11.886	9.592	7.551	7.178	72.403	54.162	38.749	28.737	20.952	15.093	10.889	8.600	7.498	7.297	7.828	8.684	9.828
33	3/1/21	15.861	13.652	11.325	8.943	6.686	5.132	11.221	69.593	47.550	34.080	24.428	17.459	12.549	9.834	8.477	8.123	8.571	9.384	10.513
34	3/11/21	15.408	13.148	10.769	8.317	5.926	3.904	3.820	65.925	58.827	40.781	28.645	20.253	14.463	11.221	9.551	9.006	9.346	10.099	11.198
35	3/21/21	14.949	12.641	10.215	7.709	5.225	2.960	1.538	8.766	70.581	49.188	33.806	23.569	16.671	12.778	10.727	9.949	10.155	10.829	11.883
36	3/31/21	14.484	12.132	9.664	7.112	4.561	2.150	0.194	0.553	62.141	59.335	40.177	27.540	19.234	14.532	12.014	10.955	10.998	11.573	12.568
37	4/10/21	14.015	11.621	9.116	6.524	3.922	1.416	-0.812	-1.994	7.170	68.699	48.044	32.353	22.236	16.519	13.430	12.031	11.877	12.333	13.254
38	4/20/21	13.542	11.109	8.569	5.943	3.301	0.728	-1.657	-3.450	-2.486	60.775	57.392	38.260	25.802	18.792	14.995	13.187	12.798	13.110	13.942
39	4/30/21	13.064	10.595	8.023	5.368	2.693	0.073	-2.412	-4.509	-5.358	6.956	66.062	45.550	30.105	21.424	16.742	14.436	13.765	13.909	14.634
40	5/10/21	12.583	10.079	7.478	4.798	2.096	-0.558	-3.109	-5.380	-6.930	-5.170	61.029	54.311	35.396	24.524	18.714	15.797	14.788	14.732	15.332
41	5/20/21	12.099	9.562	6.934	4.231	1.508	-1.172	-3.767	-6.143	-8.037	-8.468	9.016	63.065	41.999	28.251	20.974	17.294	15.877	15.585	16.038
42	5/30/21	11.611	9.043	6.391	3.668	0.927	-1.772	-4.397	-6.839	-8.922	-10.173	-7.327	61.883	50.193	32.840	23.612	18.962	17.046	16.474	16.756
43	6/9/21	11.119	8.522	5.848	3.107	0.352	-2.361	-5.005	-7.488	-9.683	-11.324	-11.206	14.843	59.331	38.634	26.763	20.851	18.315	17.407	17.490
44	6/19/21	10.625	8.000	5.305	2.549	-0.218	-2.940	-5.596	-8.105	-10.366	-12.216	-13.066	-8.804	62.540	46.073	30.636	23.033	19.709	18.394	18.245
45	6/29/21	10.127	7.477	4.762	1.993	-0.783	-3.511	-6.173	-8.696	-10.996	-12.964	-14.259	-13.492	26.008	55.258	35.560	25.617	21.266	19.450	19.025
46	7/9/21	9.626	6.951	4.219	1.438	-1.345	-4.076	-6.739	-9.268	-11.588	-13.623	-15.148	-15.531	-9.394	62.374	42.042	28.776	23.041	20.594	19.838
47	7/19/21	9.121	6.424	3.676	0.885	-1.903	-4.634	-7.296	-9.823	-12.151	-14.221	-15.872	-16.760	-15.258	40.185	50.687	32.794	25.117	21.851	20.693
48	7/29/21	8.613	5.894	3.132	0.332	-2.459	-5.188	-7.844	-10.365	-12.690	-14.776	-16.495	-17.634	-17.505	-8.814	60.399	38.164	27.627	23.262	21.603
49	8/8/21	8.102	5.363	2.587	-0.220	-3.012	-5.737	-8.384	-10.895	-13.211	-15.298	-17.049	-18.320	-18.761	-16.436	52.160	45.718	30.798	24.885	22.585
50	8/18/21	7.587	4.829	2.041	-0.771	-3.563	-6.281	-8.918	-11.414	-13.716	-15.793	-17.554	-18.892	-19.606	-18.913	-6.642	56.247	35.041	26.815	23.664

Figure 3. Values of δ targeting Mars are tabulated for year 2020 Earth departure dates. The 14.0 July 2020 UT opening date of a notional 10-day departure season (boxed) has δ_∞ = +26.822° and is selected for assessment.

The $\boldsymbol{v}_\infty$ vector for Earth departure on 14.0 July 2020 UT, leading to Type 1 Mars arrival on 30.0 January 2021 UT, is defined with J2K components in Equation (1).

$$\boldsymbol{v}_{\infty 20} = \begin{bmatrix} +3.078800 \\ +1.112367 \\ +1.647601 \end{bmatrix} \text{ km/s} \qquad (1)$$

Earth departures for Mars in 2022 are more performance-challenged than those in 2020. No Type 1 trajectory with $|\, \boldsymbol{v}_\infty \,| < 4$ km/s is available. To make matters worse, δ_∞ cannot be brought much lower than +40° without substantially increasing $|\, \boldsymbol{v}_\infty \,|$ to more than 5 km/s. The PCC pair governing selection of the 2022 Earth departure case appears in Figures 4 and 5. A notional 10-day departure season is boxed, but the actual departure case is the season-opening t_D at 9.0 September 2022 UT with $|\, \boldsymbol{v}_\infty \,|$ = 4.309 km/s. Since δ_∞ = +44.496° for this case, i = 45° is selected.

Trajectory Challenges Faced By Reusable Infrastructure In Earth Orbit Supporting Multiple Departures For Mars

◇	A	B	C	D	E	F	G	H	I	J	K	L	M	N	O	P	Q	R	S	T
1	Mars Arrive									Earth Depart Date										
2	Date	7/1/22	7/11/22	7/21/22	7/31/22	8/10/22	8/20/22	8/30/22	9/9/22	9/19/22	9/29/22	10/9/22	10/19/22	10/29/22	11/8/22	11/18/22	11/28/22	12/8/22	12/18/22	12/28/22
3	7/11/22	216.412																		
4	7/21/22	104.852	207.160																	
5	7/31/22	68.022	100.130	197.788																
6	8/10/22	49.753	64.795	95.312	188.234															
7	8/20/22	38.836	47.277	61.481	90.368	178.538														
8	8/30/22	31.559	36.819	44.718	58.057	85.355	168.631													
9	9/9/22	26.354	29.857	34.722	42.053	54.584	80.215	158.530												
10	9/19/22	22.447	24.883	28.077	32.520	39.350	51.014	74.980	148.351											
11	9/29/22	19.415	21.153	23.336	26.193	30.285	36.564	47.381	69.751	138.121										
12	10/9/22	17.006	18.261	19.787	21.688	24.279	27.977	33.730	43.786	64.536	128.043									
13	10/19/22	15.059	15.964	17.037	18.321	20.012	22.300	25.630	30.953	40.235	59.500	118.424								
14	10/29/22	13.466	14.108	14.856	15.717	16.831	18.278	20.289	23.354	28.242	36.886	54.866	109.572							
15	11/8/22	12.152	12.591	13.096	13.656	14.378	15.290	16.520	18.362	21.163	25.757	33.948	50.831	102.078						
16	11/18/22	11.065	11.340	11.658	11.995	12.442	12.995	13.733	14.858	16.540	19.225	23.709	31.590	47.810	96.614					
17	11/28/22	10.168	10.307	10.475	10.642	10.887	11.192	11.606	12.288	13.324	15.001	17.761	22.261	30.170	46.184	93.835				
18	12/8/22	9.441	9.454	9.499	9.532	9.626	9.753	9.948	10.346	10.994	12.107	13.977	16.927	21.735	29.947	47.179	94.415			
19	12/18/22	8.892	8.762	8.696	8.619	8.596	8.592	8.636	8.852	9.264	10.055	11.445	13.614	17.008	22.288	31.038	48.944	98.547		
20	12/28/22	8.601	8.225	8.042	7.870	7.754	7.653	7.592	7.691	7.963	8.576	9.709	11.465	14.143	18.062	23.914	33.490	52.572	106.053	
21	1/7/23	9.018	7.873	7.529	7.262	7.067	6.891	6.759	6.785	6.981	7.505	8.508	10.045	12.333	15.530	19.989	26.556	37.052	57.810	116.514
22	1/17/23	13.999	7.841	7.164	6.782	6.513	6.278	6.096	6.082	6.242	6.734	7.679	9.100	11.161	13.934	17.618	22.685	29.937	41.507	64.363
23	1/27/23	57.922	8.739	6.998	6.429	6.078	5.790	5.573	5.539	5.693	6.185	7.112	8.469	10.388	12.889	16.091	20.294	25.889	33.887	46.660
24	2/6/23	61.803	14.904	7.204	6.222	5.754	5.411	5.167	5.127	5.291	5.800	6.727	8.049	9.869	12.180	15.057	18.705	23.326	29.475	38.270
25	2/16/23	62.044	56.696	8.461	6.222	5.545	5.130	4.861	4.820	5.001	5.536	6.470	7.766	9.512	11.680	14.321	17.586	21.574	26.627	33.352
26	2/26/23	62.059	61.652	14.832	6.618	5.475	4.945	4.640	4.599	4.798	5.356	6.297	7.572	9.257	11.312	13.772	16.756	20.303	24.641	30.134
27	3/8/23	62.005	61.986	54.369	8.062	5.608	4.860	4.496	4.447	4.660	5.237	6.182	7.435	9.067	11.028	13.343	16.109	19.332	23.171	27.863
28	3/18/23	61.912	62.028	61.520	13.907	6.123	4.900	4.427	4.353	4.571	5.160	6.102	7.334	8.917	10.797	12.991	15.584	18.557	22.029	26.163
29	3/28/23	61.786	61.988	61.982	49.890	7.582	5.124	4.437	4.309	4.520	5.110	6.045	7.253	8.790	10.598	12.690	15.140	17.914	21.104	24.830
30	4/7/23	61.631	61.902	62.052	61.346	12.535	5.685	4.548	4.315	4.498	5.080	6.001	7.183	8.677	10.420	12.423	14.751	17.361	20.328	23.741
31	4/17/23	61.450	61.783	62.024	61.995	42.218	7.035	4.809	4.374	4.502	5.062	5.964	7.118	8.570	10.255	12.177	14.400	16.872	19.656	22.823
32	4/27/23	61.241	61.634	61.945	62.101	61.051	11.015	5.343	4.503	4.531	5.054	5.930	7.055	8.466	10.095	11.945	14.075	16.428	19.059	22.025
33	5/7/23	61.007	61.456	61.830	62.084	61.995	32.407	6.497	4.743	4.591	5.055	5.898	6.990	8.361	9.938	11.723	13.769	16.018	18.517	21.316
34	5/17/23	60.748	61.252	61.684	62.012	62.140	60.598	9.550	5.187	4.695	5.066	5.866	6.922	8.253	9.782	11.505	13.475	15.631	18.015	20.672
35	5/27/23	60.463	61.022	61.509	61.901	62.135	62.042	23.510	6.088	4.874	5.092	5.834	6.852	8.142	9.624	11.290	13.191	15.263	17.545	20.078
36	6/6/23	60.154	60.765	61.307	61.757	62.067	62.233	59.692	8.313	5.193	5.143	5.805	6.778	8.028	9.464	11.076	12.912	14.908	17.098	19.522
37	6/16/23	59.820	60.483	61.078	61.585	61.957	62.237	62.098	17.106	5.829	5.238	5.781	6.701	7.909	9.301	10.862	12.638	14.563	16.670	18.995
38	6/26/23	59.461	60.175	60.822	61.383	61.815	62.171	62.345	57.629	7.352	5.421	5.769	6.623	7.786	9.135	10.647	12.366	14.226	16.255	18.492
39	7/6/23	59.077	59.842	60.539	61.154	61.642	62.061	62.356	62.138	12.801	5.804	5.780	6.545	7.660	8.966	10.430	12.096	13.894	15.852	18.007
40	7/16/23	58.669	59.483	60.231	60.898	61.440	61.916	62.289	62.446	52.372	6.740	5.840	6.470	7.530	8.793	10.212	11.826	13.566	15.457	17.536
41	7/26/23	58.236	59.099	59.896	60.615	61.209	61.741	62.177	62.458	62.231	9.968	6.012	6.405	7.398	8.616	9.991	11.556	13.241	15.070	17.078
42	8/5/23	57.779	58.689	59.535	60.304	60.950	61.535	62.030	62.387	62.598	39.764	6.492	6.363	7.265	8.436	9.767	11.285	12.918	14.687	16.629
43	8/15/23	57.297	58.254	59.147	59.966	60.664	61.301	61.851	62.270	62.604	62.351	8.221	6.374	7.133	8.253	9.540	11.013	12.596	14.309	16.189
44	8/25/23	56.790	57.792	58.732	59.601	60.349	61.037	61.641	62.117	62.525	62.761	24.294	6.531	7.008	8.067	9.311	10.740	12.275	13.934	15.754
45	9/4/23	56.258	57.305	58.291	59.208	60.006	60.745	61.401	61.932	62.399	62.752	62.503	7.276	6.900	7.878	9.078	10.464	11.954	13.561	15.324
46	9/14/23	55.702	56.792	57.823	58.788	59.635	60.423	61.131	61.715	62.238	62.660	62.904	14.465	6.844	7.686	8.841	10.186	11.632	13.189	14.899
47	9/24/23	55.120	56.253	57.327	58.339	59.235	60.072	60.832	61.468	62.044	62.525	62.867	62.783	6.990	7.495	8.600	9.905	11.308	12.819	14.476
48	10/4/23	54.513	55.687	56.805	57.862	58.805	59.692	60.502	61.189	61.818	62.354	62.759	63.076	9.360	7.309	8.354	9.621	10.984	12.448	14.056
49	10/14/23	53.881	55.095	56.254	57.357	58.347	59.281	60.142	60.880	61.560	62.150	62.611	63.005	63.134	7.148	8.103	9.333	10.657	12.077	13.637
50	10/24/23	53.224	54.476	55.676	56.822	57.859	58.840	59.750	60.540	61.271	61.913	62.428	62.878	63.220	7.252	7.844	9.041	10.328	11.706	13.219

Figure 4. Values of | v_∞ | targeting Mars are tabulated for year 2022 Earth departure dates. The 9.0 September 2022 UT opening date of a notional 10-day departure season (boxed) has | v_∞ | = 4.309 km/s and is selected for assessment.

◇	A	B	C	D	E	F	G	H	I	J	K	L	M	N	O	P	Q	R	S	T
1	Mars Arrive									Earth Depart Date										
2	Date	7/1/22	7/11/22	7/21/22	7/31/22	8/10/22	8/20/22	8/30/22	9/9/22	9/19/22	9/29/22	10/9/22	10/19/22	10/29/22	11/8/22	11/18/22	11/28/22	12/8/22	12/18/22	12/28/22
3	7/11/22	11.145																		
4	7/21/22	13.291	13.393																	
5	7/31/22	15.093	15.337	15.411																
6	8/10/22	16.549	16.950	17.135	17.171															
7	8/20/22	17.701	18.242	18.547	18.660	18.670														
8	8/30/22	18.613	19.258	19.666	19.862	19.922	19.915													
9	9/9/22	19.352	20.065	20.543	20.805	20.919	20.943	20.915												
10	9/19/22	19.984	20.731	21.245	21.543	21.695	21.753	21.740	21.707											
11	9/29/22	20.569	21.319	21.838	22.143	22.309	22.386	22.391	22.366	22.333										
12	10/9/22	21.163	21.887	22.385	22.671	22.824	22.901	22.916	22.905	22.876	22.843									
13	10/19/22	21.824	22.488	22.940	23.185	23.306	23.363	23.372	23.371	23.356	23.326	23.301								
14	10/29/22	22.617	23.177	23.554	23.739	23.811	23.832	23.822	23.822	23.821	23.803	23.778	23.750							
15	11/8/22	23.627	24.013	24.277	24.378	24.387	24.361	24.324	24.318	24.326	24.320	24.296	24.250	24.208						
16	11/18/22	24.973	25.071	25.163	25.150	25.077	24.996	24.926	24.908	24.920	24.917	24.881	24.800	24.704	24.638					
17	11/28/22	26.845	26.449	26.275	26.101	25.922	25.776	25.668	25.633	25.638	25.619	25.540	25.386	25.195	25.040	24.940				
18	12/8/22	29.576	28.292	27.693	27.285	26.963	26.733	26.580	26.518	26.499	26.428	26.253	25.964	25.621	25.335	25.194	25.023			
19	12/18/22	33.815	30.833	29.531	28.767	28.242	27.901	27.684	27.574	27.500	27.315	26.966	26.466	25.913	25.467	25.146	25.042	24.894		
20	12/28/22	41.024	34.472	31.952	30.634	29.810	29.307	28.996	28.798	28.611	28.225	27.605	26.820	26.021	25.417	24.998	24.767	24.758	24.661	
21	1/7/23	55.009	39.967	35.215	33.002	31.727	30.984	30.522	30.173	29.786	29.085	28.098	26.980	25.940	25.211	24.735	24.496	24.431	24.501	24.478
22	1/17/23	85.430	48.892	39.755	36.043	34.072	32.966	32.266	31.668	30.966	29.827	28.402	26.948	25.709	24.909	24.423	24.213	24.197	24.253	24.402
23	1/27/23	19.597	64.715	46.341	40.016	36.952	35.296	34.228	33.251	32.099	30.413	28.523	26.771	25.396	24.578	24.121	23.966	24.015	24.132	24.292
24	2/6/23	4.430	84.233	56.412	45.339	40.522	38.029	36.413	34.896	33.153	30.844	28.507	26.518	25.067	24.270	23.867	23.779	23.897	24.076	24.296
25	2/16/23	1.179	18.445	72.576	52.692	45.010	41.247	38.837	36.589	34.125	31.160	28.421	26.255	24.773	24.020	23.679	23.660	23.844	24.080	24.351
26	2/26/23	-0.530	1.325	79.790	63.206	50.764	45.070	41.535	38.344	35.046	31.420	28.331	26.033	24.546	23.842	23.562	23.606	23.847	24.130	24.441
27	3/8/23	-1.745	-2.342	19.642	78.625	58.320	49.679	44.572	40.199	35.968	31.689	28.287	25.885	24.398	23.740	23.512	23.608	23.896	24.214	24.552
28	3/18/23	-2.734	-4.192	-1.400	77.672	68.495	55.344	48.055	42.219	36.956	32.025	28.328	25.826	24.335	23.711	23.523	23.659	23.980	24.323	24.676
29	3/28/23	-3.598	-5.462	-5.632	24.269	82.479	62.469	52.142	44.496	38.079	32.475	28.475	25.865	24.354	23.747	23.585	23.748	24.091	24.447	24.804
30	4/7/23	-4.384	-6.471	-7.643	-3.557	77.375	71.620	57.063	47.149	39.412	33.078	28.746	26.001	24.449	23.841	23.691	23.867	24.220	24.579	24.930
31	4/17/23	-5.116	-7.335	-8.966	-8.602	32.867	83.221	63.135	50.337	41.036	33.870	29.149	26.235	24.615	23.986	23.832	24.009	24.363	24.715	25.051
32	4/27/23	-5.809	-8.109	-9.984	-10.810	-4.866	77.986	70.727	54.267	43.046	34.889	29.696	26.565	24.846	24.175	24.002	24.169	24.512	24.850	25.163
33	5/7/23	-6.472	-8.822	-10.836	-12.187	-11.125	43.610	79.540	59.220	45.568	36.181	30.399	26.991	25.138	24.403	24.196	24.341	24.666	24.981	25.265
34	5/17/23	-7.111	-9.491	-11.586	-13.205	-13.577	-4.984	78.593	65.520	48.776	37.808	31.278	27.517	25.489	24.666	24.410	24.522	24.819	25.105	25.355
35	5/27/23	-7.729	-10.126	-12.268	-14.035	-15.009	-13.116	53.640	73.158	52.927	39.865	32.360	28.147	25.897	24.960	24.639	24.708	24.970	25.222	25.431
36	6/6/23	-8.331	-10.734	-12.900	-14.748	-16.020	-15.869	-3.254	77.639	58.382	42.495	33.690	28.894	26.362	25.282	24.881	24.896	25.117	25.328	25.494
37	6/16/23	-8.919	-11.319	-13.494	-15.385	-16.813	-17.353	-14.507	62.027	65.521	45.925	35.335	29.775	26.888	25.632	25.132	25.084	25.257	25.424	25.542
38	6/26/23	-9.493	-11.886	-14.058	-15.967	-17.478	-18.342	-17.631	1.600	73.333	50.534	37.405	30.820	27.482	26.009	25.392	25.270	25.388	25.506	25.574
39	7/6/23	-10.057	-12.436	-14.598	-16.507	-18.056	-19.085	-19.156	-15.238	68.735	56.929	40.085	32.073	28.151	26.412	25.657	25.451	25.508	25.574	25.590
40	7/16/23	-10.610	-12.972	-15.116	-17.014	-18.574	-19.683	-20.105	-18.799	12.243	65.764	43.701	33.611	28.914	26.844	25.925	25.624	25.615	25.626	25.588
41	7/26/23	-11.154	-13.495	-15.616	-17.493	-19.046	-20.188	-20.778	-20.343	-15.341	72.229	48.872	35.560	29.794	27.307	26.195	25.786	25.705	25.659	25.567
42	8/5/23	-11.689	-14.006	-16.100	-17.949	-19.482	-20.627	-21.293	-21.226	-19.373	31.596	56.816	38.155	30.833	27.804	26.462	25.934	25.777	25.672	25.524
43	8/15/23	-12.216	-14.506	-16.568	-18.385	-19.887	-21.016	-21.708	-21.806	-20.887	-14.892	68.811	41.872	32.100	28.344	26.723	26.061	25.825	25.660	25.458
44	8/25/23	-12.736	-14.996	-17.023	-18.801	-20.267	-21.366	-22.053	-22.220	-21.667	-19.364	52.809	47.819	33.729	28.938	26.973	26.162	25.843	25.620	25.366
45	9/4/23	-13.248	-15.476	-17.465	-19.201	-20.623	-21.683	-22.345	-22.529	-22.130	-20.770	-14.121	58.971	35.993	29.605	27.202	26.227	25.825	25.547	25.243
46	9/14/23	-13.753	-15.947	-17.895	-19.585	-20.959	-21.972	-22.595	-22.765	-22.423	-21.404	-18.813	68.707	39.576	30.381	27.397	26.241	25.760	25.432	25.085
47	9/24/23	-14.252	-16.408	-18.313	-19.954	-21.275	-22.235	-22.810	-22.947	-22.611	-21.723	-19.998	-13.428	46.747	31.344	27.534	26.181	25.631	25.265	24.885
48	10/4/23	-14.744	-16.861	-18.720	-20.308	-21.574	-22.476	-22.994	-23.086	-22.727	-21.878	-20.435	-17.782	68.782	32.689	27.564	26.012	25.418	25.034	24.633
49	10/14/23	-15.229	-17.304	-19.115	-20.649	-21.854	-22.695	-23.152	-23.188	-22.789	-21.933	-20.585	-18.606	-13.221	35.113	27.389	25.670	25.085	24.717	24.318
50	10/24/23	-15.707	-17.739	-19.498	-20.975	-22.118	-22.894	-23.285	-23.259	-22.808	-21.920	-20.589	-18.798	-16.276	44.174	26.745	25.035	24.575	24.284	23.922

Figure 5. Values of δ targeting Mars are tabulated for year 2022 Earth departure dates. The 9.0 September 2022 UT opening date of a notional 10-day departure season (boxed) has δ_∞ = +44.496° and is selected for assessment.

The $\boldsymbol{v}_\infty$ vector for Earth departure on 9.0 September 2022 UT, leading to Type 1 Mars arrival on 28.0 March 2023 UT, is defined with J2K components in Equation (2).

$$\boldsymbol{v}_{\infty 22} = \begin{bmatrix} +1.592308 \\ +2.633242 \\ +3.016596 \end{bmatrix} \text{ km/s} \tag{2}$$

4. Earth Departure Velocity Verification And Refinement For Year 2020

With $\boldsymbol{v}_{\infty 20}$ determined, the corresponding semi-minor axis b_{20} is computed from Equation (3) [4, p. 28] and Earth's reduced mass μ = 398,600.440 km^3/s^2 [2].

$$b_{20} = r \sqrt{\frac{2\,\mu}{r \left| \boldsymbol{v}_{\infty 20} \right|^2} + 1} = 21{,}172.212 \text{ km} \tag{3}$$

The 2020 departure hyperbola's β is determined from Equation (4) [4, p. 27].

$$\beta_{20} = \text{a}\tan \left\{ \frac{b_{20} \left| \boldsymbol{v}_{\infty 20} \right|^2}{\mu} \right\} = 35.504° \tag{4}$$

With $\boldsymbol{v}_{\infty 20}$ and β_{20} in hand, the 2020 TMI's LPIP is defined. Together with $\boldsymbol{v}_{\infty 20}$, each geocentric vector corresponding to a point on this LPIP defines a plane of Earth departure on 14.0 July 2020 UT. These planes are assessed to determine the one with i = 29° whose TMI has a northeasterly heading such that $0 < \psi < 90°$. The desired plane has ψ_{20} = 65.077° and Equation (5)'s geocentric J2K position at TMI.

$$\boldsymbol{r}_{20} = \begin{bmatrix} -3653.895 \\ -5422.855 \\ -1784.607 \end{bmatrix} \text{ km} \tag{5}$$

Equation (6) [4, p. 28] provides a patched conic estimate of geocentric speed following 2020's TMI.

$$v'_{20+} = \sqrt{\frac{2\,\mu}{r} + \left| \boldsymbol{v}_{\infty 20} \right|^2} = 11.447469 \text{ km/s} \tag{6}$$

It is then possible to construct a patched conic estimate of geocentric J2K velocity following 2020's TMI per Equation (7).

$$\boldsymbol{v}'_{20+} = \begin{bmatrix} +7.909101 \\ -6.855020 \\ +4.636742 \end{bmatrix} \text{ km/s} \quad (7)$$

Equation (7)'s estimate serves as an initial guess in a differential corrections iteration [5] using the trajectory modeling method described in Section 1. Each iteration starts at 14.0 July 2020 UT with Equation (5)'s TMI position, terminates at 30.0 January 2021 UT, and seeks to match heliocentric position of Mars at the terminal epoch with an error less than 1 km. Only 3 iterations are necessary to correct the Equation (7) initial velocity estimate to that given by Equation (8) and achieve the desired Mars position match. The vector difference magnitude between Equations (7) and (8) is only 0.154098 km/s. Because the differential corrections iteration rapidly converges to very nearly the patched conic estimate with which it is seeded, the two independent processes serve to mutually validate all year 2020 Earth departure results.

$$\boldsymbol{v}_{20+} = \begin{bmatrix} +7.829105 \\ -6.860184 \\ +4.768348 \end{bmatrix} \text{ km/s} \quad (8)$$

Equation (7)'s horizontal velocity is scaled to produce nearly circular apsis heights averaging +400 km (H_A = +400.7 km and H_P = +399.3 km). The resulting geocentric J2K velocity appears in Equation (9) and is adopted as that of LEO infrastructure at the TMI epoch 14.0 July 2020 UT.

$$\boldsymbol{v}_{20-} = \begin{bmatrix} +5.301064 \\ -4.594568 \\ +3.107770 \end{bmatrix} \text{ km/s} \quad (9)$$

Magnitude of the vector difference between Equations (8) and (9) is equivalent to Δv_{TMI} = 3.779091 km/s. Due to the correction in post-TMI velocity applied to Equation (7) in obtaining Equation (8), Δv_{TMI} reflects a small TMI steering angle of 0.771° from the purely prograde thrust direction.

Earth departure geometry for 14.0 July 2020 UT consistent with that described in Section 2 is illustrated in the Figure 6 CSP using Equations (1), (4), (5), and (9) values. This departure case's LPIP is also plotted in Figure 6.

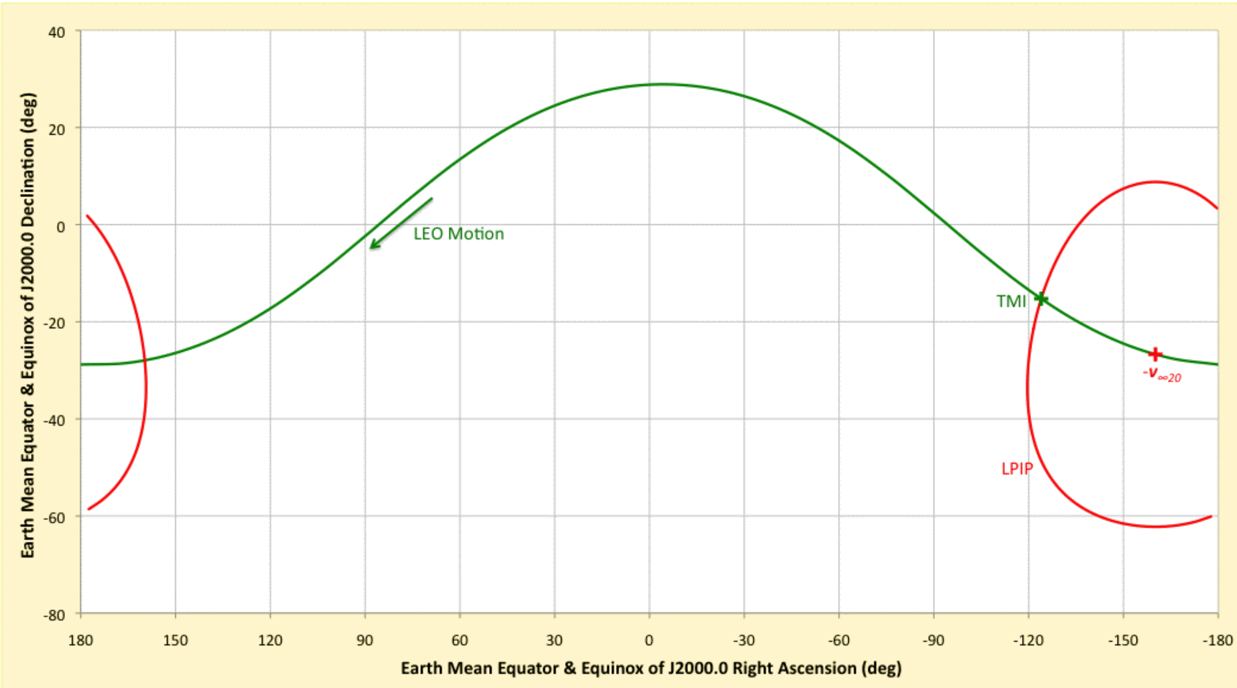

Figure 6. A LEO plane with i = 29° (green line) supporting prograde Earth departure for Mars on 14.0 July 2020 UT is projected onto the geocentric J2K celestial sphere. Note infrastructure motion in the LEO plane passes through $-v_{\infty 20}$ (red +) before reaching TMI (green +) on a northbound heading. The geocentric arc from $-v_{\infty 20}$ to TMI is β_{20}.

5. Year 2020 LEO Coast To Year 2022

The trajectory modeling method described in Section 1 is supplied with LEO initial conditions at the 14.0 July 2020 UT Earth departure epoch obtained from Equations (5) and (9). A simulated LEO coast to the 9.0 September 2022 UT Earth departure epoch is then performed. Terminal geocentric J2K conditions from this coast appear in Equations (10) and (11).

$$\boldsymbol{r}_{20\rightarrow 22} = \begin{bmatrix} +3944.059 \\ +4465.877 \\ -3230.562 \end{bmatrix} \text{ km} \qquad (10)$$

$$\boldsymbol{v}_{20\rightarrow 22} = \begin{bmatrix} -5.455183 \\ +5.344323 \\ +0.728862 \end{bmatrix} \text{ km/s} \qquad (11)$$

The coast's terminal conditions show the LEO's apses to be little changed from the initial near-circular orbit at +400 km height (H_A = +401.1 km and H_P = +399.7 km). This consistency is expected from not simulating LEO atmospheric drag during the coast, and it reasonably approximates infrastructure orbit lifetime maintenance operations. Likewise, i = 28.977° is obtained at the coast's terminal epoch, indicating LEO inclination is well preserved during the two-year interval. In contrast, LEO right ascension of the ascending node (RAAN) has been dynamic throughout the coast due almost entirely to torques exerted by J_2 perturbations.

To illustrate LEO planar motion during the coast, osculating geocentric angular momentum normal to the plane is projected onto the geocentric J2K celestial sphere at daily intervals in Figures 7-10. These CSPs are narrow strips in declination, each vertical axis spanning only 0.3°. Magnified vertical scaling reveals minute variations in declination as angular momentum precesses a full 360° in right ascension over cycles about 50 days in duration[‡]. Each of these 4 CSPs in turn plots 4 precession cycles color-coded in a chronological sequence of blue diamonds, orange squares, green triangles, and purple dots. The start of each UT calendar month, together with the two Earth departure epochs, is annotated with the corresponding date in Figures 7-10.

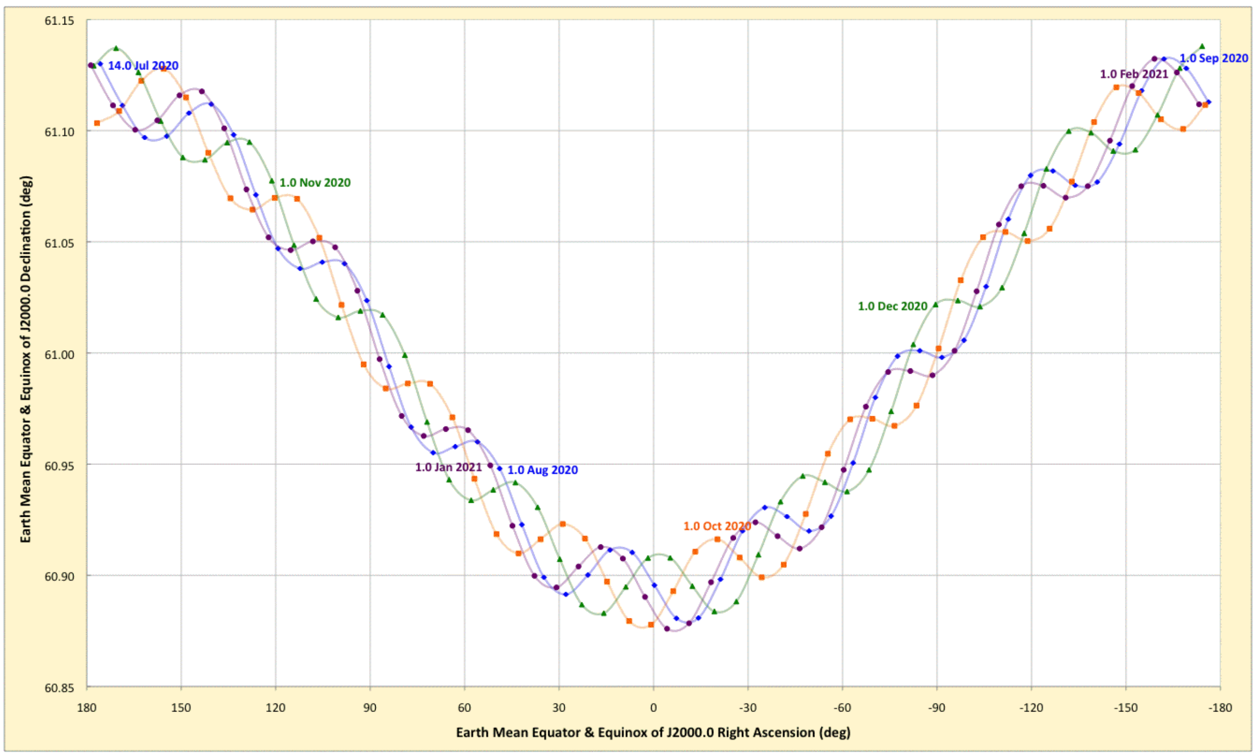

Figure 7. The coasted LEO's osculating geocentric angular momentum vector is projected onto the geocentric J2K celestial sphere at daily intervals from 14.0 July 2020 UT to 2.0 February 2021 UT.

‡ Note that, in the context of this paper's prograde LEO, the angular momentum vector's declination with respect to Earth's true equator is simply 90° - i because i is also defined with respect to Earth's true equator. In contrast, all CSPs have declination plotted with respect to the J2K equator. Therefore, although i = 29° at the 14.0 July 2020 Earth departure epoch, the Figure 7 initial point at that epoch has a J2K declination of +61.130°, slightly different from its true declination of 90° - 29° = +61°.

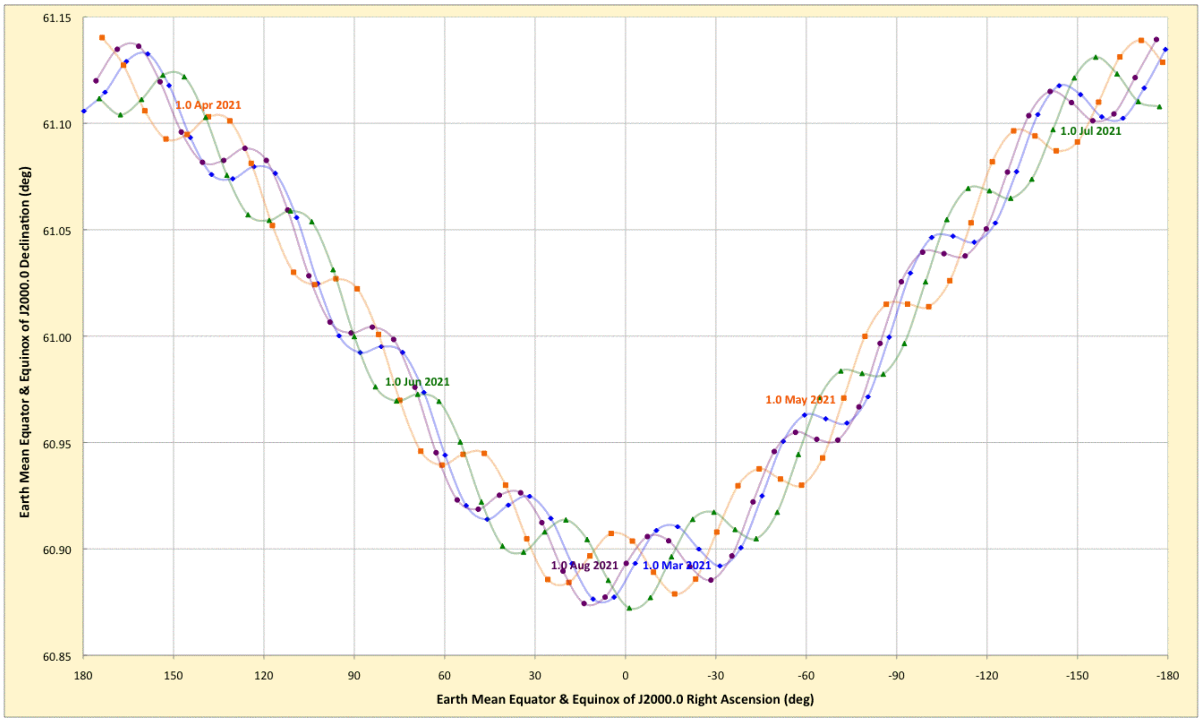

Figure 8. The coasted LEO's osculating geocentric angular momentum vector is projected onto the geocentric J2K celestial sphere at daily intervals from 3.0 February 2021 UT to 26.0 August 2021 UT.

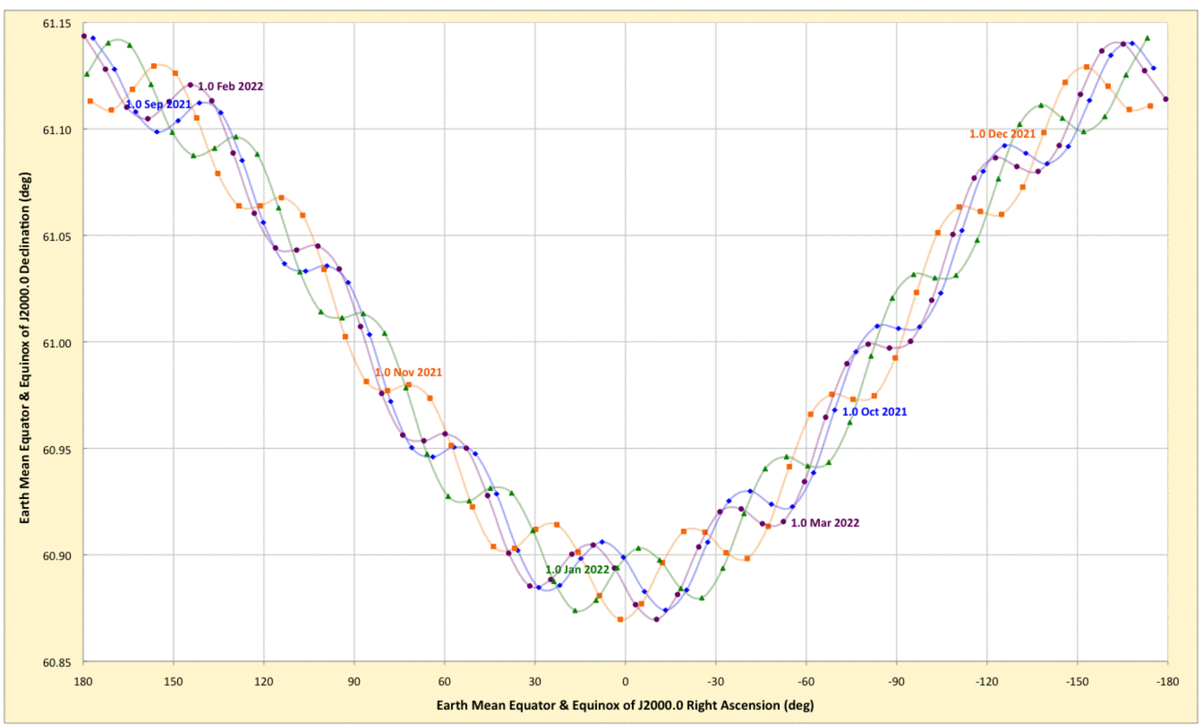

Figure 9. The coasted LEO's osculating geocentric angular momentum vector is projected onto the geocentric J2K celestial sphere at daily intervals from 27.0 August 2021 UT to 19.0 March 2022 UT.

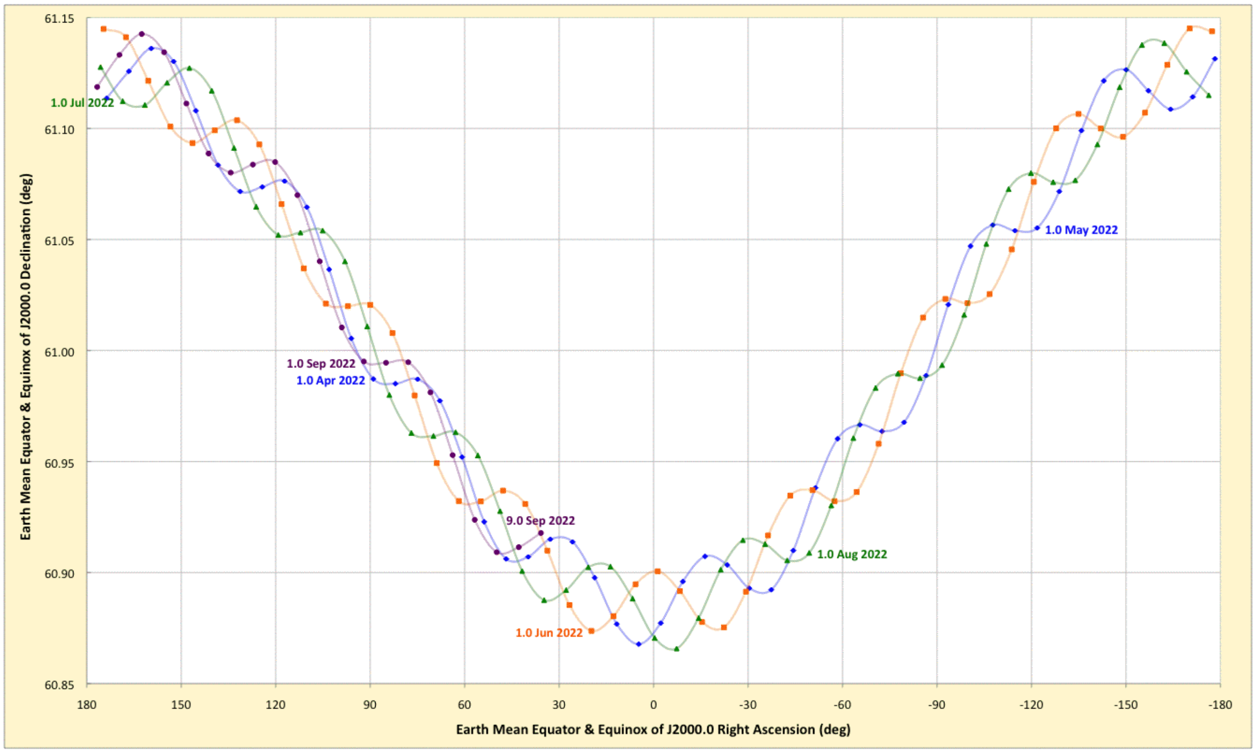

Figure 10. The coasted LEO's osculating geocentric angular momentum vector is projected onto the geocentric J2K celestial sphere at daily intervals from 20.0 March 2022 UT to 9.0 September 2022 UT.

Angular momentum variations in declination evident in Figures 7-10 arise from two distinct sources. The first of these is due to the J_2 perturbation's force component acting normal to the coasted LEO plane [6, p. 567]. But this torque averages zero over the interval between successive Earth true equator crossings, about 46.2 min in the coasted LEO. Nevertheless, polling the coasted LEO at differing points in its half-orbit J_2 cycle influences daily angular momentum computations reflected in Figures 7-10. Variations depending on sampling the J_2 cycle amount to 0.035° (peak-to-valley) in CSP declination and are easily resolved by the magnified vertical scale common to Figures 7-10. At 31.169 J_2 cycles per day, 6 days are required to sample all portions of a J_2 cycle at daily intervals. Thus, the higher frequency declination variations seen in Figures 7-10 are partially attributable to an artifact: relatively infrequent sampling of a periodic J_2 cycle having no net effect over intervals more than 0.8 hrs.

The sinusoidal variation in declination whose amplitude spans the vertical axis in Figures 7-10 is due to another artifact. This variation would disappear if coasted LEO angular momentum were plotted on a celestial sphere whose declination is with respect to Earth's true equator. On such a CSP, J_2-induced precession in the angular momentum vector would be about an axis parallel to the CSP declination axis. But J2K declination is inclined to true declination during the LEO coast by about 0.12°, giving rise to a 0.24° peak-to-valley declination variation during each 50-day precession cycle in Figures 7-10.

Moon and Sun gravitational forces also contain components normal to the coasted LEO plane. But a LEO is small in scale and short in period compared to lunar/solar distances and their geocentric motions. Consequently, these perturbations only impart miniscule changes on the order of 0.01° to the coasted LEO plane's terminal orientation when compared with a coast having only J_2 perturbations. Even near the LEO coast's terminal conditions, planar deviations in a coast without Moon/Sun perturbations would barely be resolved in Figure 10 and only by the highly magnified declination scale.

6. Earth Departure Velocity Verification And Refinement For Year 2022

With $\boldsymbol{v}_{\infty 22}$ determined, the corresponding semi-minor axis b_{22} is computed from Equation (12) [4, p. 28] and Earth's reduced mass μ = 398,600.440 km^3/s^2 [2].

$$b_{22} \;=\; r \sqrt{\frac{2\,\mu}{r\,\left|\,\boldsymbol{v}_{\infty 22}\,\right|^{2}} \;+\; 1} = 18{,}355.837 \text{ km} \tag{12}$$

The 2022 departure hyperbola's β is determined from Equation (13) [4, p. 27].

$$\beta_{22} \;=\; \text{a}\tan\left\{\frac{b_{22}\,\left|\,\boldsymbol{v}_{\infty 22}\,\right|^{2}}{\mu}\right\} = 40.535° \tag{13}$$

With $\boldsymbol{v}_{\infty 22}$ and β_{22} in hand, the 2022 TMI's LPIP is defined. Together with $\boldsymbol{v}_{\infty 22}$, each geocentric vector corresponding to a point on this LPIP defines a plane of Earth departure on 9.0 September 2022 UT. These planes are assessed to determine the one with i = 45° whose TMI has a northeasterly heading such that $0 < \psi < 90°$. The desired plane has ψ_{22} = 53.317° and Equation (14)'s geocentric J2K position at TMI.

$$\boldsymbol{r}_{22} \;=\; \begin{bmatrix} +1628.976 \\ -5748.410 \\ -3200.836 \end{bmatrix} \text{ km} \tag{14}$$

Equation (15) [4, p. 28] provides a patched conic estimate of geocentric speed following 2022's TMI.

$$v'_{22+} \;=\; \sqrt{\frac{2\,\mu}{r} \;+\; \left|\,\boldsymbol{v}_{\infty 22}\,\right|^{2}} = 11.669741 \text{ km/s} \tag{15}$$

It is then possible to construct a patched conic estimate of geocentric J2K velocity following 2022's TMI per Equation (16).

$$\boldsymbol{v}'_{22+} = \begin{bmatrix} +9.914678 \\ -0.601150 \\ +6.125409 \end{bmatrix} \text{ km/s} \tag{16}$$

Equation (16)'s estimate serves as an initial guess in a differential corrections iteration [5] using the trajectory modeling method described in Section 1. Each iteration starts at 9.0 September 2022 UT with Equation (14)'s TMI position, terminates at 28.0 March 2023 UT, and seeks to match heliocentric position of Mars at the terminal epoch with an error less than 1 km. Only 3 iterations are necessary to correct the Equation (16) initial velocity estimate to that given by Equation (17) and achieve the desired Mars position match. The vector difference magnitude between Equations (16) and (17) is only 0.088261 km/s. Because the differential corrections iteration rapidly converges to very nearly the patched conic estimate with which it is seeded, the two independent processes serve to mutually validate all year 2022 Earth departure results.

$$\boldsymbol{v}_{22+} = \begin{bmatrix} +9.870252 \\ -0.640011 \\ +6.191030 \end{bmatrix} \text{ km/s} \tag{17}$$

Equation (16)'s horizontal velocity is scaled to produce nearly circular apsis heights averaging +400 km (H_A = +401.6 km and H_P = +398.4 km). The resulting geocentric J2K velocity appears in Equation (18) and is adopted as that of LEO infrastructure at the TMI epoch 9.0 September 2022 UT.

$$\boldsymbol{v}_{22-} = \begin{bmatrix} +6.516679 \\ -0.395121 \\ +4.026084 \end{bmatrix} \text{ km/s} \tag{18}$$

Magnitude of the vector difference between Equations (17) and (18) is equivalent to Δv_{TMI} = 3.999177 km/s. Due to the correction in post-TMI velocity applied to Equation (16) in obtaining Equation (17), Δv_{TMI} reflects a small TMI steering angle of 0.433° from the purely prograde thrust direction.

Earth departure geometry for 9.0 September 2022 UT consistent with that described in Section 2 is illustrated in the Figure 11 CSP using Equations (2), (13), (14), and (18) values. This departure case's LPIP is also plotted in Figure 11, together with the LEO plane coasted from 14.0 July 2020 UT to 9.0 September 2022 UT as defined by terminal conditions from Equations (10) and (11).

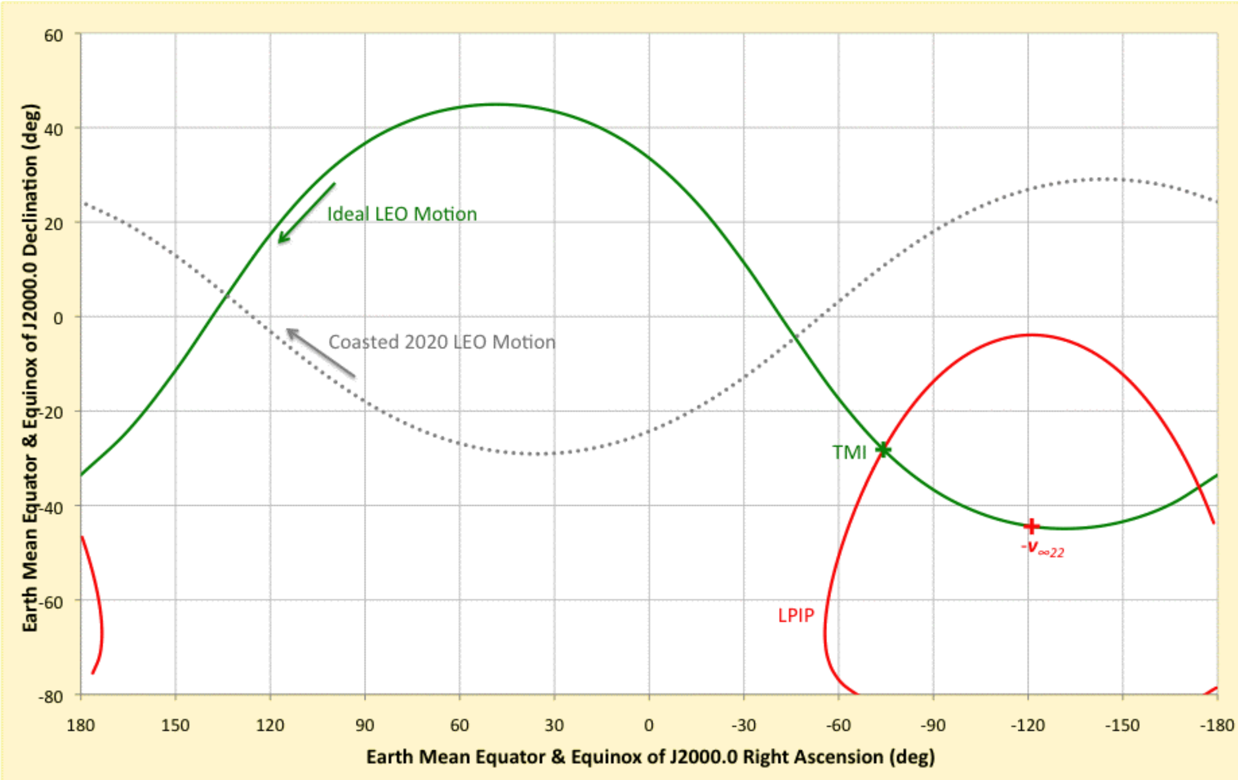

Figure 11. An ideal LEO plane with i = 45° (green line) supporting prograde Earth departure for Mars on 9.0 September 2022 UT is projected onto the geocentric J2K celestial sphere. Note infrastructure motion in the LEO plane passes through $-v_{\infty 22}$ (red +) before reaching TMI (green +) on a northbound heading. The geocentric arc from $-v_{\infty 22}$ to TMI is β_{22}, and the dotted gray line is the LEO plane coasted in Section 5 from an ideal Earth departure for Mars on 14.0 July 2020 UT.

The wedge angle between ideal and coasted LEO planes plotted in Figure 11 is 73.500°. This angle can be zeroed with a single planar correction impulse Δv_{PC} = 9.180 km/s at either of the two intersection points, or nodes, between the two planes evident in Figure 11. Such a correction exceeds Δv_{TMI} and even surpasses geocentric speed in either LEO per Equations (11) and (18). More sophisticated strategies, with which orbiting infrastructure supporting the 2020 Earth departure can also support the 2022 Earth departure, are suggested in Section 7.

7. Reuse Strategies Covering Multiple Earth Departure Seasons For Mars

Although the reusable infrastructure assembles and services massive payloads prior to each payload's departure for Mars, this infrastructure may be highly maneuverable when free of payload obligations. The following subsections suggest strategies to maneuver infrastructure in support of multiple servicing campaigns. These strategies are presented in the context of achieving ideal Earth departure geometry for Mars during years 2020 and 2022 as developed in Sections 3, 4, and 6.

7.1 Alter LEO *H* To Obtain A Desired RAAN

As illustrated in Figure 11, the ideal J2K RAAN to depart Earth for Mars at i = 45° on 9.0 September 2022 UT is -41.677°, while J2K RAAN on that date coasted from an ideal departure at i = 29° on 14.0 July 2020 UT is +125.706°. Subtracting the coasted RAAN from the ideal 2022 RAAN produces a desired J2K RAAN shift $\Delta\Omega$ = -167.383° (negative $\Delta\Omega$ signifies a westward RAAN shift). If this shift could be imparted during the 2020-to-2022 coast, wedge angle between the two planes would be reduced to the difference in their J2K inclinations, or 44.915° - 29.079° = 15.836°. The smaller wedge in turn reduces Δv_{PC} to 2.114 km/s.

In a prograde orbit, planar precession due to J_2 results in a westward RAAN drift over time. The rate of RAAN drift increases in magnitude with decreasing orbit height and decreasing inclination [6, pp. 591-592]. Consequently, when the 14.0 July 2020 UT state vector from Equations (5) and (9) is scaled to produce nearly circular apsis heights averaging +342.5 km (H_A = +343.2 km and H_P = +341.8 km) while retaining i = 29°, a coast to 9.0 September 2022 UT achieves $\Delta\Omega$ = +0.009°. Initial and terminal geocentric J2K states for this coast appear in Equations (19) through (22).

$$\boldsymbol{r}_{\Omega 20} = \begin{bmatrix} -3622.886 \\ -5376.834 \\ -1769.462 \end{bmatrix} \text{ km} \tag{19}$$

$$\boldsymbol{v}_{\Omega 20} = \begin{bmatrix} +5.323751 \\ -4.614231 \\ +3.121070 \end{bmatrix} \text{ km/s} \tag{20}$$

$$\boldsymbol{r}_{\Omega 20 \rightarrow 22} = \begin{bmatrix} +1453.064 \\ -6236.516 \\ -2038.688 \end{bmatrix} \text{ km} \tag{21}$$

$$\boldsymbol{v}_{\Omega 20 \rightarrow 22} = \begin{bmatrix} +7.104015 \\ +0.705419 \\ +2.900428 \end{bmatrix} \text{ km/s} \tag{22}$$

The coasted orbit plane in Figure 11 is replaced by that defined with Equations (21) and (22) in Figure 12. Note that the Δv_{PC} impulse required to increase i to 45° must occur at the coasted plane's nodes with the ideal Earth departure plane (which are also the coasted LEO's nodes on the J2K equator in this case) and therefore cannot be combined with Δv_{TMI}.

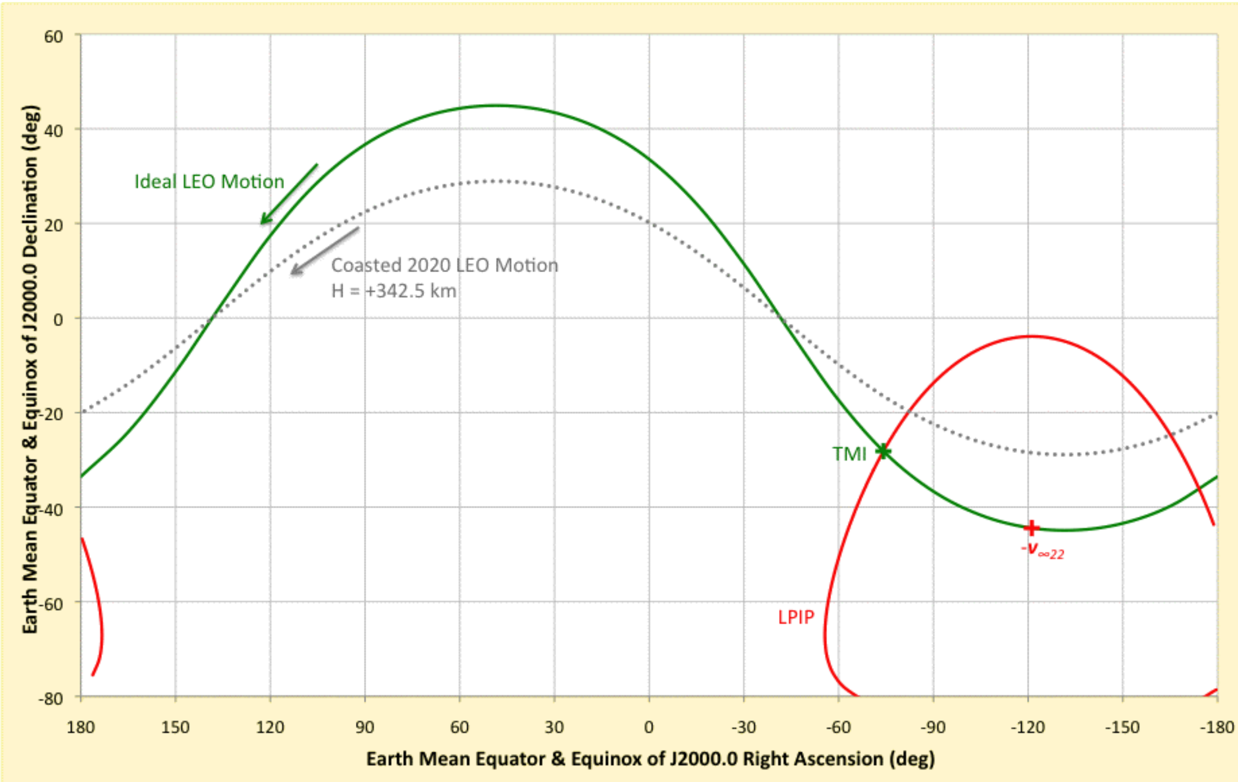

Figure 12. Ideal Earth departure geometry for Mars on 9.0 September 2022 UT is reproduced from Figure 11. Height associated with the LEO plane coasted from 14.0 July 2020 UT has been lowered from +400 km in Figure 11 to +342.5 km (dotted gray line) in order to match J2K RAAN with that of the ideal LEO.

In addition to propellant required to lower the coasted orbit to $H = +342.5$ km (and possibly return it to $H = +400$ km), this strategy requires more propulsion to counteract orbit decay due to atmospheric drag than would a LEO at greater H. Massive payload servicing at $H < +400$ km may by inadvisable. Only during early phases of its assembly was the International Space Station (ISS) orbit permitted to decay down to H near +320 km (reference http://www.nasa.gov/mission_pages/shuttle/shuttlemissions/archives/sts-101.html). Together with its highly maneuverable mass, prolonged reduced solar activity (and the reduced atmospheric density it imparts) facilitated flying the nascent ISS in such low orbits.

Assuming freedom from payload obligations to coast at H appreciably different from +400 km over more than two years to achieve a RAAN match could be highly optimistic. Massive payload servicing near +400 km (or some other standard H) may dictate the coast performed in this subsection instead be conducted at an even lower H over a more curtailed interval between servicing obligations at the higher standard H.

There is also a reverse strategy to that developed by this subsection in which an easterly J2K RAAN shift $\Delta\Omega = 360° - 167.383° = +192.617°$ is conducted with $H > +400$ km. This strategy enjoys reduced atmospheric drag with respect to lower orbit heights, but it also suffers increased radiation flux from particles trapped in Earth's magnetosphere. Because this flux is harmful to human health and spacecraft systems, ISS is rarely operated at $H > +430$ km. Such a constraint would not leave much of an orbit height envelope in which to shift RAAN eastward with respect to a coast at $H = +400$ km.

7.2 Utilize An Elliptical Earth Parking Orbit (EEPO)

An EEPO offers opportunities to take advantage of two fundamental astrodynamics techniques. At apogee, geocentric speed is at a minimum, and a required plane change can be achieved with minimal Δv_{PC}. At perigee, geocentric speed is at a maximum, and Δv_{TMI} can be dramatically reduced from the corresponding impulse in LEO [7]. Fully realizing this "Oberth effect" presumes the TMI geometry described in Section 2, together with perigee located at TMI.

As a context for applying these techniques by example, consider an EEPO with $i = 29°$ and $H_P = +400$ km at 14.0 July 2020 UT. Position for this EEPO example is $\boldsymbol{r}_{20}$ from Equation (5), and geocentric J2K velocity is $\boldsymbol{v}_{20-}$ from Equation (9) scaled to produce a geographic longitude of ascending node on Earth's true equator (LAN) repetition every two days. This condition also causes rendezvous phase angles to repeat on that cycle, standardizing planning and flight procedures associated with massive payload logistics to the reusable infrastructure. The repeated LAN is near 28° W with ascending node passages at 00:15:19 UT on 12 July 2020 and 00:06:30 UT on 14 July 2020 bracketing the TMI epoch. Figure 13 illustrates motion in the EEPO between these two node passages. Scaled $\boldsymbol{v}_{20-}$ in the EEPO at perigee on 14.0 July 2020 UT is given by Equation (23), producing $H_A = +121{,}639.3$ km.

$$\boldsymbol{v}_{20\text{-}EEPO} = \begin{bmatrix} +7.302022 \\ -6.328849 \\ +4.280839 \end{bmatrix} \text{km/s} \tag{23}$$

Raising apogee about a third of the way to the Moon's orbit is a launch vehicle performance challenge compared to LEO, and it applies to logistics throughout the entire massive payload assembly and servicing campaign. But this challenge also permits much of the kinetic energy required for TMI to be generated soon after each massive payload element is launched using efficient cryogenic propellant. To perform TMI with cryogenic propellant from a circular LEO would require low temperature storage in that thermally challenging environment, likely over a time interval measured in months to a year or more.

Consider a maximum plane change of 90° performed during EEPO apogee passage on 13 July 2020 at 00:04:30 UT. Geocentric speed at this point is 0.565 km/s, and the 90° $\Delta v_{PC} = 0.798$ km/s. This is a dramatic reduction from a similar impulse in an $H = +400$ km circular orbit, but it may not be the maximum Δv_{PC} required to rotate the EEPO plane 90°. In general, the line of nodes between the EEPO and the desired orbit plane will not lie along the EEPO line of apsides. Therefore, a less optimal geometry could require shifting the plane change impulse well away from apogee to locations where higher geocentric speeds prevail. The node closer to apogee is the plane change's preferred location in order to minimize geocentric speed and Δv_{PC}.

Geocentric speed at the EEPO perigee is 2.896 km/s greater than that in a circular H = +400 km orbit, reducing the 14.0 July 2020 UT Δv_{TMI} by a similar amount to 0.893 km/s. This impulse again includes a small TMI steering angle of 0.771° from the purely prograde thrust direction.

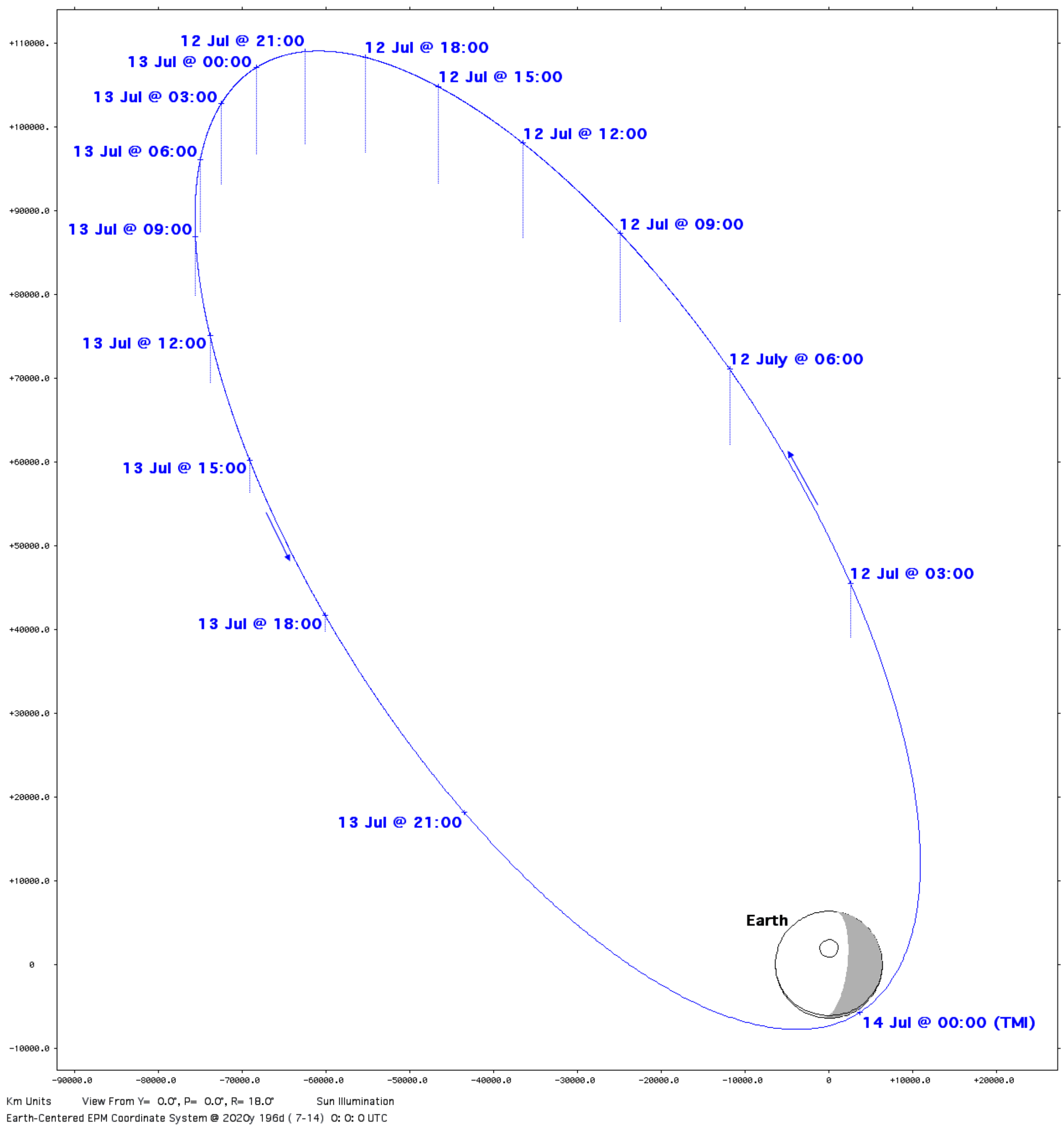

Figure 13. Geocentric inertial motion is plotted in an EEPO with *i* = 29° and H_A x H_P = +121,639.3 km x +400 km as viewed nearly normal to the plane of motion. The plot spans successive Earth true equator ascending node passages bracketing the 14.0 July 2020 UT perigee at which TMI would be performed. Time tick annotations are UT, dotted lines are projections onto Earth's true equatorial plane, and the shaded area is Earth's nightside.

The Figure 13 EEPO passes through regions with some of the highest trapped particle radiation flux in Earth's magnetosphere (reference the Trapped Radiation section at http://srag-nt.jsc.nasa.gov/SpaceRadiation/What/What.cfm). If the reusable infrastructure or massive payload destined for Mars is radiation-sensitive, EEPO perigee can be raised to evade regions with unacceptable particle fluxes. In this case, apogee can also be raised to maintain desirable LAN repetition properties of the Figure 13 EEPO.

If perigee must be raised appreciably from $H = +400$ km, taking full advantage of the Oberth effect will likely entail lowering it back just before TMI. In the context of Earth departure for Mars, it actually requires less propellant to lower EEPO perigee and perform TMI than it does to perform TMI directly from a higher perigee. For a typical EEPO with 2-day period, the break-even point between these two competitive strategies is near $| \boldsymbol{v}_\infty | = 2$ km/s. At $| \boldsymbol{v}_\infty | > 2$ km/s, lowering perigee as much as possible for TMI is propellant-efficient. Per $| \boldsymbol{v}_\infty |$ data in Figures 2 and 4, the "lowest possible H at TMI" strategy definitely applies to Earth departures for Mars in years 2020 and 2022. A relatively small perigee-lowering impulse, performed about a day before TMI to maximize the Oberth effect, can in practice also serve as a useful test of the TMI propulsion system before committing a massive and presumably costly payload (possibly carrying a crew) to Mars transit.

In contrast to an $H = +400$ km circular LEO, a 2-day EEPO experiences appreciable Moon and Sun gravity perturbations. Left uncontrolled, these can significantly alter orbit elements, including inclination and apsis heights, between successive Mars departure seasons. For example, coasting the Figure 13 EEPO to 9.0 September 2022 UT produces an orbit with i = 25.334° and H_A x H_P = +121,737.0 km x -664.706 km. This decayed orbit outcome, even in the absence of atmospheric drag, is another argument in favor of long-term EEPO maintenance at H_P considerably above +400 km. When drag is considered, higher perigee in an EEPO virtually eliminates its energy-robbing effects until shortly before TMI.

7.3 Loiter In A Selenocentric Distant Retrograde Orbit (DRO)

This strategy requires a trans-lunar injection (TLI) impulse whose magnitude can be approximated by requiring $| \boldsymbol{v}_\infty | = 0$ post-TLI. In this discussion, the initial and final orbits are assumed to be EEPOs supporting purely prograde TMI impulses during two different Earth departure seasons. Application of this strategy to TMIs from LEO would entail considerably larger impulses than its application to TMIs from EEPO and is therefore inadvisable except to address unplanned contingencies.

Following massive payload servicing obligations in EEPO, the reusable infrastructure will loiter there for at least a few months awaiting sufficient alignment of its line of apsides with the Sun/Earth line. Geometry relevant to this alignment is illustrated in Figure 13, with the EEPO perigee initially located at a local solar time of approximately 8 PM. As Earth revolves about the Sun in the months following Figure 13's TMI, EEPO perigee will approach local solar noon. At this point, it will be possible for a near-perigee TLI impulse about 0.28 km/s in magnitude to send the infrastructure on a trajectory closely approaching the second Sun/Earth libration point (SEL2), about 1.5 million km (or 1%) outside Earth's heliocentric orbit. Transit past SEL2 is designed to satisfy two objectives. First, it incurs solar gravity perturbations causing infrastructure geocentric total energy to more closely match the Moon's. Second, a coasted return to the Moon's vicinity is targeted to occur near lunar last-quarter phase such that selenocentric speed is minimal.

Loitering an additional six months in EEPO would place perigee sufficiently close to local solar midnight, and a near-perigee TLI impulse about 0.28 km/s in magnitude could send the infrastructure on a trajectory closely approaching the first Sun/Earth libration point (SEL1), about 1.4 million km inside Earth's heliocentric orbit. This TLI targets return to the Moon's vicinity near its first-quarter phase. A similar technique was applied to achieve lunar orbit for the twin Gravity Recovery And Interior Laboratory (GRAIL) spacecraft and is illustrated in Figure 14 from downloaded as-flown trajectory data [2].

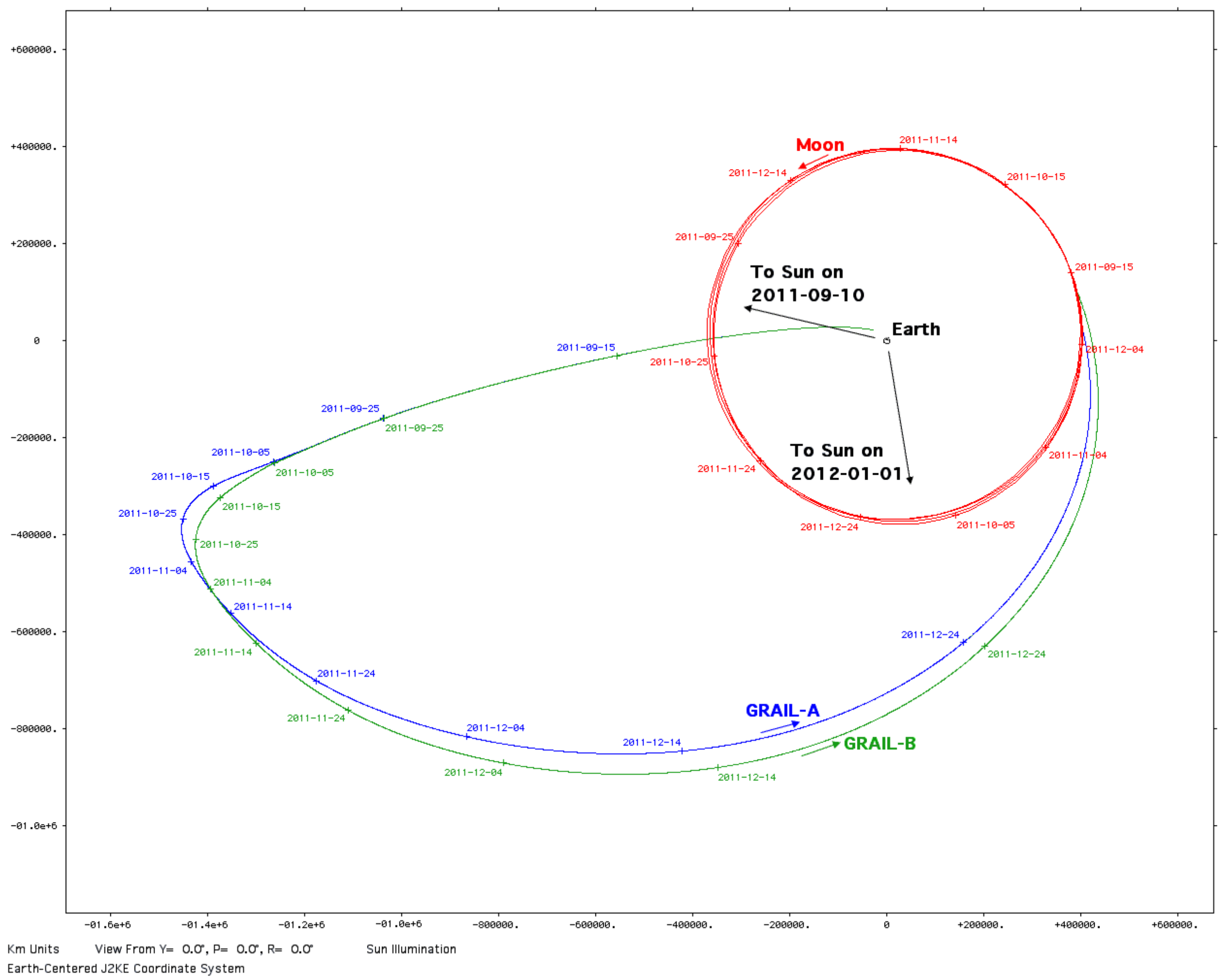

Figure 14. Geocentric as-flown GRAIL trajectories (blue and green) are plotted in the inertial ecliptic plane. Time tick labels are in year-month-day format. Note how solar perturbations to these trajectories cause them to intercept the Moon's orbit (red) tangentially so as to minimize selenocentric speed and achieve lunar orbit with minimal propulsion.

Per Figure 14's GRAIL example, arrival at the Moon's vicinity can be expected about 4 months after TLI. Research supporting near-Earth asteroid redirection into a stable selenocentric DRO indicates DRO insertion from a slow lunar approach can be achieved with an impulse approximately 0.1 km/s in magnitude [8].

Depending on future servicing obligations, the reusable infrastructure may safely loiter in the DRO for decades, straying no more than about 70,000 km from the Moon. If those obligations are relatively immediate, however, the DRO loiter interval may be shortened to less than a month. In general, DRO departure must occur at the proper time of the lunar month to ensure a subsequent EEPO is established with its perigee located on the LPIP and its plane containing $\boldsymbol{v}_\infty$ at TMI in accord with Section 2 geometric constraints. Conic transfer from the Moon's orbit to H_P = +400 km requires a trans-Earth injection (TEI) impulse about 0.83 km/s in magnitude[§], and lowering apogee of the resulting orbit to 120,000 km, thus establishing a 2-day EEPO, requires an impulse about 0.19 km/s in magnitude. Table 1 summarizes an approximate and expedited timeline example for the selenocentric DRO loiter strategy.

Table 1. Phase Elapsed Time (PET) is measured in months since a massive payload performs TMI after assembly and servicing by reusable infrastructure in an initial EEPO. The infrastructure then undergoes a trajectory recycling process to achieve the correct EEPO for a subsequent TMI at 26 months PET. This process entails loitering in the initial EEPO and in a selenocentric DRO. After recycling to the second EEPO, the infrastructure has 16 months in which to assemble and service a second massive payload before it departs Earth for Mars.

PET (months)	Event
0	First Earth departure season TMI. Begin loiter in supporting EEPO.
4	Depart EEPO for SEL2 flyby with 0.28 km/s TLI impulse.
8	Return to Moon and achieve 70,000 km radius DRO with 0.1 km/s impulse.
9	Perform 0.57 km/s TEI impulse and establish 2-day EEPO supporting second Earth departure season with 0.19 km/s impulse several days later.
10	Begin servicing operations for second Earth departure season TMI.
26	Second departure season TMI.

Other researchers have proposed similar trajectory recycling strategies. For example, Farquhar advocates loitering at SEL2 to reuse Earth/Mars transport infrastructure [9, Chapter 15].

[§] This TEI impulse magnitude estimate assumes no lunar gravity must be overcome to achieve lunar escape and is consistent with a circular selenocentric DRO of radius 70,000 km near the Moon's gravitational sphere of influence. A TEI impulse of 0.83 km/s is also thought to be near a mean value because zero selenocentric speed is assumed pre-TEI. But a 70,000 km DRO has selenocentric speed near 0.26 km/s. Therefore, a TEI targeted to occur near the Earth/Moon line 70,000 km beyond the Moon's geocentric orbit could have a reduced impulse of 0.83 - 0.26 = 0.57 km/s.

8. Conclusions

A scenario has been documented in which reusable infrastructure in Earth orbit assembles and services a massive payload departing for Mars in 2020. The infrastructure remains in space to repeat this task in 2022. Geometric constraints governing the infrastructure's orbit for the two Earth departure seasons have been presented and shown to require dramatically different planar orientations. These conflicting trajectory constraints pose formidable challenges to infrastructure reuse.

If infrastructure is based in circular LEO, a large wedge angle develops with respect to the Earth departure orbit plane required in 2022 when the Earth departure orbit plane in 2020 is coasted to 2022. Some of this wedge angle can be removed by deviating from the reuse scenario's specified LEO height to target the required 2022 departure RAAN. Even if this technique is practical, a dedicated inclination plane change impulse about 2 km/s in magnitude is necessary to zero the wedge angle. Placing infrastructure in LEO to support the reuse scenario is therefore not recommended.

As an alternative to LEO, reusable infrastructure based in an EEPO with period near 2 days is proposed. This orbit permits much of the propulsive energy required to depart Earth for Mars to be expended only hours after a massive payload element is launched to achieve infrastructure rendezvous, thereby vastly reducing departure cryogenic propellant storage requirements. The EEPO plane is easily rotated if plane change impulses can be placed near apogee. In lieu of that circumstance, the EEPO provides access to Moon and Sun perturbations capable of achieving the desired 2022 Earth departure EEPO in approximately 10 months using impulses totaling about 1 km/s. Consequently, the infrastructure reuse scenario during years 2020 into 2022 favors Earth departure for Mars from a 2-day EEPO.

To avoid excessive radiation exposure from particles trapped in Earth's magnetic field, minimize atmospheric drag orbit energy losses, and evade orbit decay, EEPO perigee must be sufficiently high. It may then be necessary to lower the massive payload's perigee to a minimal safe height immediately prior to TMI. Only at the minimum practical perigee will the payload be taking maximum advantage of the Oberth effect's propulsive efficiency at TMI.

References

[1] Adamo, D. R., "A Precision Orbit Predictor Optimized For Complex Trajectory Operations," *Astrodynamics 2003, Advances in the Astronautical Sciences*, Vol. 116, Univelt, San Diego, CA, 2003, pp. 2567-2586.

[2] Giorgini, J. D., Yeomans, D. K., Chamberlin, A. B., Chodas, P. W., Jacobson, R. A., Keesey, M. S., Lieske, J. H., Ostro, S. J., Standish, E. M., Wimberly, R. N., "JPL's On-Line Solar System Data Service", *Bulletin of the American Astronomical Society*, Vol. 28, No. 3, p. 1158, 1996.[**]

[3] Rockwell International Space Systems Division, "Orbital Altitude Time Task", *Space Shuttle Orbiter Operational Level C Functional Subsystem Software Requirements Guidance,*

[**] For further information on using this service, see http://ssd.jpl.nasa.gov/?horizons (accessed 6 June 2013).

Navigation, And Control Part A Guidance Ascent/RTLS, STS 83-0002G, OI-24, April 15, 1993.
[4] Brown, C. D., *Spacecraft Mission Design*, American Institute of Aeronautics and Astronautics, Inc., 1992.
[5] Adamo, D. R., "Apollo 13 Trajectory Reconstruction via State Transition Matrices", *Journal of Guidance, Control, and Dynamics*, Vol. 31, No. 6, AIAA, 2008, pp. 1772-1781.
[6] Vallado, D. A., *Fundamentals of Astrodynamics and Applications*, McGraw Hill, 1997.
[7] Oberth, H. J., *Ways to Spaceflight* [translation of *Wege zur Raumshiffahrt*, R. Oldenbourg Verlag, Munich-Berlin, 1929], NASA TT F-622, 1970, p. 200.
[8] Landau, D., Dankanich, J., Strange, N., Bellerose, J., Llanos, P., Tantardini, M., "Trajectories to Nab A NEA (Near-Earth Asteroid)", AAS 13-409.[††]
[9] Farquhar, R. W., *Fifty Years On The Space Frontier: Halo Orbits, Comets, Asteroids, And More*, Outskirts Press, 2011.

[††] This paper may be downloaded from http://www.kiss.caltech.edu/study/asteroid/GetaNEA_2-4-13.pdf (accessed 29 June 2013).